SDOF Solution for the response of gravity loaded walls subjected to blast load

GENGSHENG WANG

FOI-R--5202--SE
ISSN 1650-1942

August 2022

Gengsheng Wang

SDOF Solution for the response of gravity loaded walls subjected to blast load

Titel	SDOF Solution for the response of gravity loaded walls subjected to blast load
Title	Enfrihet lösning för axiell-belastad betong vägg
Rapportnr/Report no	FOI-R--5202--SE
Månad/Month	Augusti
Utgivningsår/Year	2022
Antal sidor/Pages	51
ISSN	1650-1942
Uppdragsgivare/Client	FortV
Forskningsområde	Vapen, Skydd och säkerhet
FoT-område	Inget FoT-område
Projektnr/Project no	E21404
Godkänd av/Approved by	Henric Östmark
Ansvarig avdelning	Vapen, skydd och säkerhet

Sammanfattning

I detta arbete utvecklas en lösning för analys av ett gravitationsbelastat väggelement som utsätts för luftstötvåg från sprängladdning. Lösningen är baserad på vidareutveckling av den konventionella metoden för analys med hjälp av ett enfrihetsgradssystem (SDOF) för dynamisk responsanalys av strukturella komponenter. Gravitationsbelastningen appliceras på toppen av väggen med en motsvarande massa. Både kriterierna för böj- och skjuvbrott ingår i lösningen när den axiella belastningseffekten beaktas. Lösningen valideras med finit elementmetodanalys och några experimentella data för att utforska potentialen för allmänna utvärderingar av dynamisk respons hos en gravitationsbelastad vägg som utsätts för luftstötsvågsbelastning.

Nyckelord: byggnader, luftstötsvåg, SDOF, gravitation, axial belastning, betongvägg.

Summary

In this work, a solution for the response of a gravity loaded wall element subjected to blast load is developed. The solution is based on the extension of the conventional single-degree-of-freedom (SDOF) method for the dynamic response analysis of structural components. The gravity axial load is applied on the top of the wall with an equivalent mass. Both the bending and shear failure criteria are included in the solution when the axial load effect is accounted for. The solution is validated with finite element analyses and some experimental data to explore potential of the solution for general engineering evaluations of the dynamic response of a gravity loaded wall subjected to the blast load.

Keywords: Blast, SDOF, gravity load, axial loaded, walls, reinforced concrete.

Contents

1 Introduction

For many buildings, the walls are constructed to carry the gravity load from the floors and roofs above them. Failure of such load bearing walls are often catastrophic, likely leading to the collapse of the construction.

While structure elements such as the load bearing columns have received significant research efforts [1-13], the research on the load bearing walls are rather limited and inadequate [14-15]. The construction guidelines and rules often do not cover the load bearing walls [16] when they are subjected to severe airblast load.

During the transient blast load from an explosion of high explosives or gases, walls often experience significant pressure with very short durations in the time scale of miliseconds. The response of the walls will become very complex and differ significantly from that for static loads. Various experiments have indicated that the gravity load along the walls will significantly affect the response of the walls [17]. Design rules based on the quasi-static interaction diagram [16] are inadequate to ensure a reliable analysis of the dynamic response of the load bearing walls.

Unlike the load bearing columns that are designed to carry significant gravity load and often having large thickness to height ratio, the walls often are relatively thin, compared to their width. For an explosion event, the main concerns for the columns are often the close and contact detonations that cause great local damages. The blast pressure against a wall surface will be a major concern due to the large surface area and small thickness. In addition, the reinforcement is often different for the walls compared to that for the load bearing columns.

To understand the failure behavior of load bearing walls, experiment series have been performed [14-15]. These experiments indicated significant effect of the axial load on the response of the walls under the blast loading condition.

Various numerical simulations based on the explicit dynamic code have been performed to analyze the experimental results [18-20]. It is shown that the numerical simulations are capable of capturing characteristics of the dynamic response of various reinforced concrete structures. The simulations are however rather complex and time consuming. For a timely evaluation, reasonable sizing tools and construction guidelines are needed. To establish guidelines, parametric studies are needed to investigate the effect of various parameters. Such work will need reliable fast-running solutions.

The single degree of freedom solution (SDOF [21-24]) seems to be a good candidate for the analyses of wall response under the blast loading condition. In this work, the conventional SDOF solution is extended to include the gravity effect for the analysis of the characteristics of the load bearing walls under the blast loading condition. The solution is validated with both the experimental results from [14-15] and numerical simulations.

2 SDOF solution

The equivalent single degree of freedom (SDOF) model is based on the energy equivalence of the actual and the single degree dynamic systems. The method has been developed since the 50's. It has been proved that the solution is a reasonable method for a timely evaluation of the dynamic response of structural elements under the blast loading conditions [22-24].

With this solution, the actual pressure, mass, and stiffness of the wall ($p(t)$, M, and K) are transformed into the equivalent force, mass, stiffness ($F_e(t)$, M_e, and K_e), and damping characteristics (c_e) for a SDOF system as shown schematically in Fig.1.

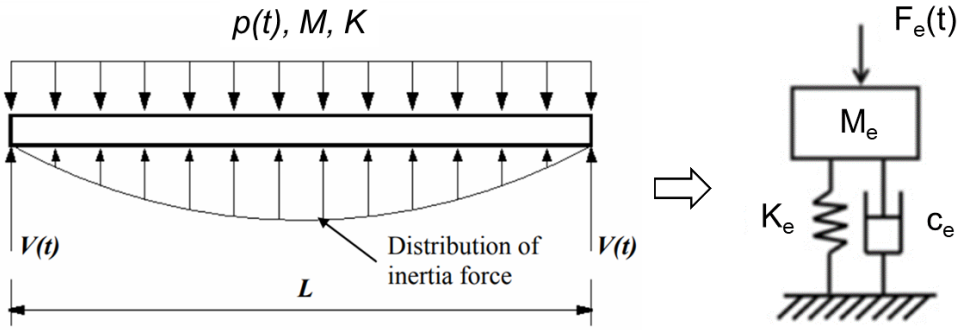

Figure 1: Schematic of the single degree of freedom (SDOF) representation of the dynamic structural response.

The dynamic response of the structural element is approximated with a one-dimensional analytical solution of:

$$M_e \frac{d^2w}{dt^2} + c_e \frac{dw}{dt} + K_e w = F_e(t) \quad (1)$$

where w is the characteristic movement of the structure. w can be used to respresent the the maximum deflection of the structure. The keys for this solution is to determine the equivalent quantities for the mass (M_e), stiffness (K_e), force (F_e), and the damping coefficient (c_e). The energy equivalence is considered so that the equivalent system will have the same energy balance as the structure [25].

2.1 Energy equivalence

To establish a SDOF system for the structural response analyses of a component, the following steps [23][25] is considered:

1) Assume an appropriate deformed shape of the structural component

2) Differentiate the deformed shape to obtain strains

3) Substitute the strains into the appropriate relationship for strain energy per unit volume

4) Integrate the strain energy per unit volume over the volume of the structural element to obtain the total strain energy

5) Compute the kinetic energy

6) Compute the maximum work by integrating over the loaded area for the pressure times the deflection

7) Obtain the deformation by equating the work and kinetic energy to the strain energy, and

8) Substitute deformation into strain equation to obtain strains in the structure element.

2.2 SDOF of walls

It is assumed that the wall will have its thickness and maximum deflection considerably smaller than its height. The equivalent system is chosen so that the movement of the equivalent mass is the same as the maximum deflection of the wall. To consider a deflection function $\phi(x,t)$ for the neutral axis of a wall such as:

$$\phi(x,t) = w_0(t) f(x/L) \quad (2)$$

In this equation, the height of the wall is L and the length coordinate is x. $w_0(t)$ is a characteristic deflection magnitude (the maximum deflection), and $f(x/L)$is the deflection shape function for $0 < f(x/L) < 1$. It is a dimensionless function of the deformation of the wall for $0 < x < L$.

The external work done by a blast load on the surface of the wall with a pressure distribution of $p(x,t) = N(x)g(t)$ is computed by the integration of the pressure multiplied by the deflection according to:

$$W = \int_0^L N(x)g(t)\phi(x)dx \quad (3)$$

In this equation:

$N(x)$: is the pressure distribution function,

$g(t)$: is the time history of the blast load,

$\phi(x)$: is the wall deflection function (the shape function).

With a shape function $f(x/L)$ for the deflection, the external work W is determined by the following integration.

$$W = g(t)w_0(t)L\int_0^1 N(x')f(x')dx' \quad (4)$$

In this equation, $x' = x/L$ is a normalized coordinate along the axis of the wall.

For a uniform pressure on the surface of the wall, $p(x,t) = N(x)g(t) = p(t)$, The external work is determined by:

$$W = p(t)Lw_0\int_0^1 f(x')dx' = p(t)Lw_0K_L \quad (5)$$

In this equation, K_L is a geometry constant determined by the shape function according to:

$$K_L = \int_0^1 f(x')dx' \quad (6)$$

The kinetic energy ($K.E.$) of the wall is determined by integrating the mass and velocity of the wall:

$$K.E. = \frac{1}{2}\int_0^L m(x)\left[\frac{d}{dt}\phi(x)\right]^2 dx \quad (7)$$

In this equation, $m(x)$ is the distribution of mass along the length of the wall.

Again, this equation is defined according to the dimensionless shape function $f(x')$:

$$K.E. = \frac{1}{2}\left(\frac{dw_0}{dt}\right)^2 L\int_0^1 m(x')[f(x')]^2 dx' \quad (8)$$

For a uniformly distributed mass along the length of the wall. The solution for kinetic energy during the deflection becomes:

$$K.E. = \frac{1}{2}\left(\frac{dw_0}{dt}\right)^2 M\int_0^1 [f(x)]^2 dx = \frac{1}{2}\left(\frac{dw_0}{dt}\right)^2 MK_M \quad (9)$$

In this function, M is the total mass, and K_M is a geometry constant determined by the shape function according to:

$$K_M = \int_0^1 [f(x')]^2 dx' \quad (10)$$

During the dynamic deflection, the strain energy $S.E.$ of the beam is determined by the beam theory based on the curvature of the deflection along the wall according to:

$$S.E. = \frac{1}{2}\int_0^L EI(x)\left[\frac{d^2}{dx^2}\phi(x)\right]^2 dx \quad (11)$$

For a given deflection function of $f(x')$, eq.(11) is solved:

$$S.E. = \frac{1}{2L^3}w_0^2(t)\int_0^1 EI(x')[f''(x')]^2 dx' \quad (12)$$

For the wall with a constant section along its length, $EI(x) = EI = const.$, the strain energy is determined by:

$$S.E. = \frac{EI}{2L^3} w_0^2(t) \int_0^1 [f''(x')]^2 dx' = \frac{EI}{2L^3} w_0^2(t) K_K \quad (13)$$

Again in this equation, K_K is a geometry constant determined by the shape function according to:

$$K_K = \int_0^1 [f''(x')]^2 dx' \quad (14)$$

For the wall subjected to a blast load, the external work on the corresponding SDOF system should be:

$$W = F_e w_0 \quad (15)$$

With w_0 as a characteristic displacement determined by the equivalence of work according to:

$$F_e g(t) \phi_0 = \int_0^L N(x) g(t) \phi(x) dx \quad (16)$$

The equivalent force for the blast load $p(t)$ will be determined with the constant K_L determined by eq.(6):

$$F_e w_0 = p(t) L w_0 K_L \quad (17)$$

This gives a solution for the equivalent force F_e:

$$F_e = p(t) L K_L = K_L P(t) \quad (18)$$

Here, $P(t) = \int_0^L N(x) g(t) dx$ is the total force on the surface of the wall.

The equivalent kinetic energy of the wall for the SDOF system is defined by the characteristic displacement ϕ_0 and the equivalent mass M_e according to:

$$K.E. = \frac{1}{2} M_e \left(\frac{d\phi_0}{dt}\right)^2 \quad (19)$$

The equivalent kinetic energy of the SDOF (eq.(19)) should be equal to the kinetic energy of the wall:

$$K.E. = \frac{1}{2} M_e \left(\frac{d\phi_0}{dt}\right)^2 = \frac{1}{2} \left(\frac{dw_0}{dt}\right)^2 M K_L \quad (20)$$

Assume the displacement of the SDOF representing the maximum deflection of the wall ($\phi_0 = w_0$), the equivalent mass M_e is solved:

$$M_e = K_M M \tag{21}$$

The equivalent strain energy of the SDOF is defined by:

$$S.E. = \frac{1}{2} K_e w_0^2 \tag{22}$$

The equivalent strain energy should be equal to the strain energy of the wall according to:

$$S.E. = \frac{1}{2} K_e w_0^2 = \frac{EI}{2L^3} w_0^2 K_K \tag{23}$$

The equivalent stiffness of SDOF is thus solved according to:

$$K_e = K_K \frac{EI}{L^3} \tag{24}$$

According to the beam theory, the sectional bending moment in the wall is determined for small deflection based on the curvature:

$$M_{bending} = EI \frac{d^2}{dx^2} \phi(x) \tag{25}$$

With the shape function $f(x')$, the bending moment is determined with the curvature of the deformation ($f''(x)$) by:

$$M_{bending} = w_0 \frac{EI}{L^2} f''(x') \tag{26}$$

The equivalent SDOF dynamic system of the wall will be determined by a motion function of:

$$M_e \frac{d^2 w_0}{dt^2} + c_e \frac{dw_0}{dt} + K_e w_0 = F_e(t) \tag{27}$$

For the wall, the equivalent motion function becomes:

$$K_M M \frac{d^2 w_0}{dt^2} + c_e \frac{dw_0}{dt} + K_K \frac{EI}{L^3} w_0 = K_L p(t) L \tag{28}$$

As long as the shape function $f(x')$ is deterimined, K_M, K_K, and K_L are determined according to eq.(21), eq.(14), and eq.(6). The single degree equivalent dynamic system is determined by eq.(27-28) for the characteristic deflection of the wall, w_0, as a function of time for a blast pressure of $p(t)$.

When the SDOF method first was proposed [23][25], the computational capability and experimental evidence was inadequate, the dynamic damping was often ignored for the following arguments:

1) Only one cycle of response of the structure was of interest.

2) In one cycle, the attenuation of the response produced by structural damping is small.

3) Ignoring damping is a conservative approach.

4) Damping values for structures are seldom known.

5) The energy dissipated through plastic deformation is much greater than that dissipated by normal structural damping.

However, the blast pressure due to detonation of explosives is often characterized with very high magnitude and short duration. For such a load, the effect of system damping will often be significant. Today, the computational capability has been significantly improved. Many experiments have indicated the importance of the damping in the response. With an asymmetrically reinforced wall, the response during several cycles has often to be considered to capture the rebound failure that may occur for certain types of blast load. None of the above arguments will be defendable anymore.

To include the damping effect will greatly improve the understanding of the structural response under the blast loading condition. In this work, the damping effect is included for the SDOF solution.

2.3 Reaction force

It is not unusual to consider the shear failure for the walls subjected to the blast load [26-27]. The shear failure may sometimes reduce the resistance of a wall against blast load [28-29]. To study the shear failure, the reaction forces at the supports of the wall have to be considered.

During the blast load, the reaction force of the wall consists of both the inertial and reaction force. For a simple supported wall, a schematic of the forces on the wall is shown in Fig. 2. In this figure, $Ng(t)$ is the blast pressure, and $V(t)$ is the reaction force on the support. Only a part of the beam is considered in the figure covering the distance of X until the shear force becomes zero. Within this section, the maximum inertial force occurs at the location with the largest deflection.

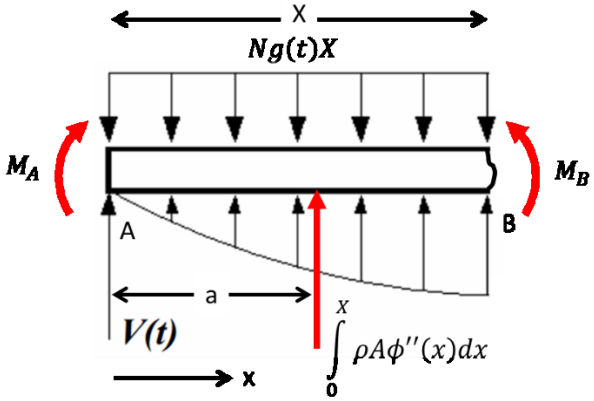

Figure 2: Schematic of the forces acting on a supported wall under the dynamic loading condition.

The inertia forces is determined by the acceleration of the wall according to:

$$F_{Inertia} = \int_0^X \rho A\phi''(x)dx \tag{29}$$

In this equation, A is the cross sectional area of the wall and ρ is the density of the wall. X is the distance along the wall from the support to where the shear force becomes zero. For example for the simply supported wall subjected to a uniform pressure, the shear force will become zero at $X = L/2$.

Consider the moment equilibrium with respect to the inertia force center for section X. There is a condition of:

$$V(t)a + M_A - M_B - p(t)X\left(a - \frac{X}{2}\right) = 0 \tag{30}$$

In this equation, $p(t) = Ng(t)$ is the blast pressure. $V(t)$ is the reaction force at the support, M_A is the sectional bending moment on the left hand end at the support, and M_B is the sectional bending moment at a distance X from the support. a is the center of inertia force. Eq.(30) gives a general solution for the reaction force at the support:

$$V(t) = \frac{M_B - M_A}{a} + p(t)X\left(1 - \frac{X}{2a}\right) \tag{31}$$

To determine the center a of inertia force, the deformation function of the wall has to be considered. At the location through the center of inertia load, the equilibrium of bending moment requires:

$$\int_0^a \rho A\ddot{\phi}(x)(a - x)dx - \int_a^X \rho A\ddot{\phi}(x)(x - a)dx = 0 \tag{32}$$

This gives a solution for the center of inertia force:

$$\frac{a}{L} = \frac{\int_0^{X/L} f(x')x'dx'}{\int_0^{X/L} f(x')dx'} \quad (33)$$

In this function, $f(x')$ is the shape function of the wall. For example for a symmetrical deflection with respect to the center of the wall, the reaction force at the support is solved as:

$$V(t) = \frac{3(M_B - M_A)}{2X} + \frac{X}{4}p(t) \quad (34)$$

According to this solution, the reaction force will be determined by the pressure $p(t)$, the shear free distance X , and the sectional moment at the support and at X. For multiple supported walls, the sectional moment M_A and M_B are determined by the curvature of the shape function according to eq.(26).

2.4 Numerical solution

The general SDOF motion function is governed by:

$$\frac{d^2w(t)}{dt^2} + 2\beta\frac{dw(t)}{dt} + \omega_0^2(t)w(t) = f(t) \quad (35)$$

In this equation:

$\beta = \frac{c}{2m(t)}$: is the half of the damping parameter

$\omega_0 = \sqrt{\frac{k(t)}{m(t)}}$: is the nominal frequency

$f(t) = \frac{p(t)}{m(t)}$: is the nominal load

$m(t)$: is the mass as a function of time for the SDOF system

$k(t)$: is the stiffeness of the SDOF

The damping in eq.(35) accounts for the viscous effect due to the movement (velocity) of the mass. The damping may be further characterized with a damping coefficient ζ defined by the nominal frequency ω_0 of the motion equation:

$$\beta = \zeta\omega_0 \quad (36)$$

The damping coefficient has a value range $\zeta = 0 - 1$. For $\zeta = 0$ there will be no damping in the system while for $\zeta = 1$, the system will be fully damped. It is generally accepted that for buildings, damping coefficient falls between 2 percent and 10 percent of critical damping value ($\zeta = 0.02 - 0.1$).

The basic dynamic system becomes:

$$\frac{d^2w(t)}{dt^2} + 2\zeta\omega_0(t)\frac{dw(t)}{dt} + \omega_0^2(t)w(t) = f(t) \quad (37)$$

Generally, the equation has to be solved numerically when the coefficient for the mass, nominal frequency, and damping are a function of the force $f(t)$, time t and movement $w(t)$. There are many different time integration numerical methods to solve the above function. In this work, the average acceleration method is used [30].

To solve the dynamic system numerically, the simulation period is determined at first according to the number of response periods n needed to be studied:

$$t\_end = n(2\pi)/\omega_0 \tag{38}$$

The time step for the numerical simulation is determined with the total steps N according to:

$$\Delta t = \frac{n(2\pi)}{\omega_0 N} \tag{39}$$

The numerical solution consists of the following steps.

Step 1. At $t = 0$: compute the initial acceleration based on the initial pressure and mass:

$$\ddot{w}(0) = \frac{p(0)}{m(0)} \tag{40}$$

For this step, the initial velocity and displacement are given for $\dot{w}(0) = 0$ and $w(0) = 0$.

Step 2. Increment for a time step to $t = t + \Delta t$,

Step 3. At $t = t + \Delta t$, compute the acceleration according to:

$$\ddot{w}_t = \frac{1}{m+\frac{1}{2}c\Delta t+\frac{1}{4}k\Delta t^2}\left[f(t) - k\left(w_{t-\Delta t} + \dot{w}_{t-\Delta t}\Delta t + \frac{1}{4}\ddot{w}_{t-\Delta t}\Delta t^2\right) - c\left(\dot{w}_{t-\Delta t} + \frac{1}{2}\ddot{w}_{t-\Delta t}\Delta t\right)\right] \tag{41a}$$

The velocity is determined by the acceleration according to:

$$\dot{w}_t = \dot{w}_{t-\Delta t} + \frac{1}{2}(\ddot{w}_t + \ddot{w}_{t-\Delta t})\Delta t \tag{41b}$$

The displacement is determined by:

$$w_t = w_{t-\Delta t} + \frac{1}{2}(\dot{w}_t + \dot{w}_{t-\Delta t})\Delta t \tag{41c}$$

Step 4. Repeat Step 2 and Step 3 until t_end defined by eq.(38).

Note that if $w_{t=0}$ and $\dot{w}_{t=0}$ are zero, the mass will not move as long as $p(t) = 0$. However when $f(t) \neq 0$, eq.(40) will give an acceleration and the motion will start. Thus, this system of equations is self-starting and requires no special starting provisions.

3 Gravity effect

For walls subjected to the gravity load from the upper structure, the SDOF solution in Section 2.2 has to be modified to take account for the effect of gravity. A reasonable simplification is to consider the wall subjected to the gravity load from a mass acting at the top, equivalent to the mass of the upper structures that the wall has to bear, see the right hand side of the schematic as shown in Fig.3.

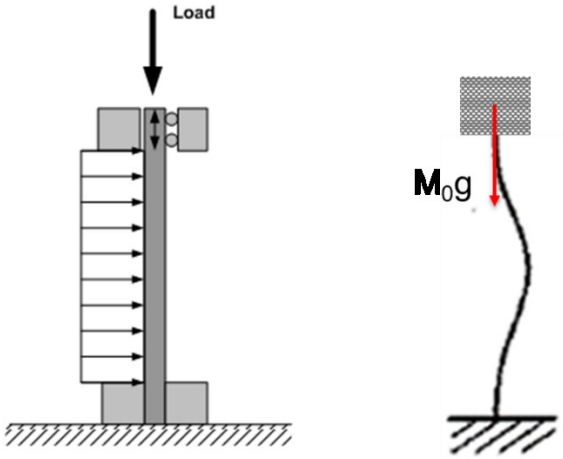

Figure 3: Schematic of the simplification for a gravity loaded wall.

During the bending of the wall, the height of the wall will change due to the horizontal deflection of its axis, leading to acceleration of the mass above the wall. The acceleration will create an inertia force in the mass that may significantly change the axial force acting on the top of the wall. This effect may be negligible for a quasi-static load, but for a blast load, considerable acceleration may occur on the mass and the load on the top of the wall can be significantly different from that for a static loading condition.

3.1 Mass movement

Two major types of the axial displacement of the mass are considered. When the wall is subjected to the blast pressure, the height of the wall will change due to the transverse deflection (bending) of the wall. There will also be an arching effect due to the rigid rotation of the wall. The arching effect is illustrated in Fig.4. In this paper the former is called the flexural axial displacement, and the latter (rigid rotation) is called the arching displacement.

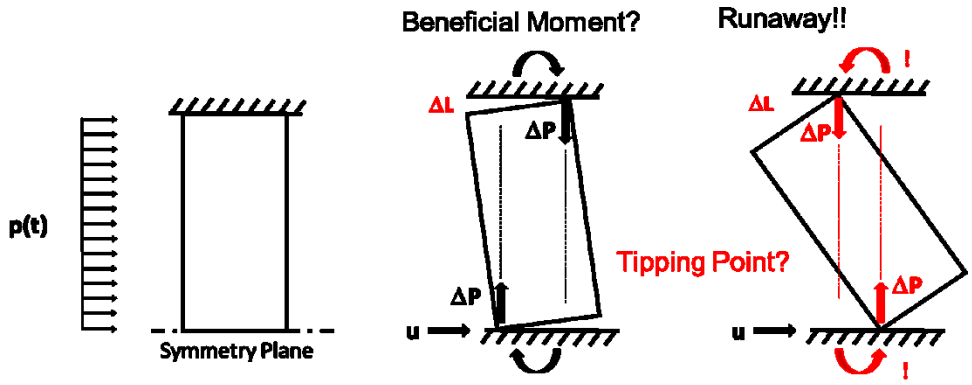

Figure 4: Deflection due to arching effect,the rigid rotation of the axis.

For the flexural displacement, the axial dimension of the neutral axis is considered. For a given deflection $w = \phi(x)$, the axial dimension of the beam is determined by an integral of:

$$S = \int_0^L dS = \int_0^L \sqrt{1 + \left(\frac{dw}{dx}\right)^2}\, dx \tag{42}$$

With a series extension, the differential length dS is approximated according to:

$$dS = dx\sqrt{1 + \left(\frac{dw}{dx}\right)^2} = dx\left[1 + \frac{1}{2}\left(\frac{dw}{dx}\right)^2 - \frac{1}{2\cdot 4}\left(\frac{dw}{dx}\right)^4 + \cdots\right] \tag{43}$$

At small curvature (dw/dx), the length given in eq.(42) may be approximate with the first two terms of the series extension of eq.(43):

$$S \approx \int_0^L \left[1 + \frac{1}{2}\left(\frac{dw}{dx}\right)^2\right] dx \approx L + \frac{1}{2}\int_0^L \left(\frac{dw}{dx}\right)^2 dx \tag{44}$$

The axial flexural displacement of the neutral axis δ_0 is then approximated according to:

$$\delta_0 = S - L = \frac{1}{2}\int_0^L \left(\frac{dy}{dx}\right)^2 dx = \frac{1}{2L} w_0^2 \int_0^1 [f'(x')]^2 dx' = \frac{1}{2L} K_A w_0^2 \tag{45}$$

This axial displacement will be determined with a constant:

$$K_A = \int_0^1 [f'(x')]^2 dx' \tag{46}$$

This parameter is determined by the shape function $f(x')$ of the wall.

The axial displacement will consist of both the deflection of the neutral axis, and the displacement due to the arching effect. According to the model as shown in Fig.4, the deflection due to arching may be approximated by considering the rigid rotation of the wall due to non-uniform transverse deflection. Due to the rigid rotation, an axial displacement δ_{arch}will occur at the end. The displacement can be approximated by:

$$\delta_{arch} = \frac{2D}{d}|w_0|\left(1 - \frac{|w_0|}{2d}\right) \tag{47}$$

In this function, D is approximated according to:

$$D = \sqrt{l_0^2 + d^2} - l_0 \tag{48}$$

Here, l_0 is the Euler's effective length and d is the thickness of the wall. The length l_0 will depend on the bending mode.

The arching effect occurs after the rigid rotation. This effect will be affected by plastic yield or tension failure. The equivalent axial movement of the mass is thus determined by both the flexural and arching displacement according to:

$$\delta_{axial} = \begin{cases} 0 & \text{after tension failure} \\ -\delta_0 & \text{after plastic yield} \\ \delta_{arch} - \delta_0 & \text{otherwise} \end{cases} \tag{49}$$

From eq.(45) and eq.(48), the elastic axial displacement will be expressed as:

$$\delta_{axial} = \frac{2D}{d}|w_0|\left(1 - \frac{|w_0|}{2d}\right) - \frac{1}{2L}K_A w_0^2 \tag{50}$$

This displacement is determined by both the shape (K_A) and deflection (w_0) of the wall.

3.2 Eigenvalue

The axial load will change the nature frequency of the wall. For a beam subjected to an axial compression, Galef [31] gives an equation for the response frequency. Due to the axial load T, the nature frequency of the beam will be changed to:

$$\omega(T) = \omega_0\left(1 + \frac{T}{P_{buckling}}\right)^{1/2} \tag{51}$$

In this equation, T is the axial load and $P_{buckling}$ is the Euler's elastic buckling load for the wall. The buckling load is determined by:

$$P_{buckling} = \frac{\pi^2 EI}{l_0^2} \tag{52}$$

Again, l_0 in this equation is the Euler's effect beam length.

Further improvement is made by Bokaian [32] to introduce a parameter γ_b to account for the effect of tension for a more general case:

$$\omega(T) = \omega_0 \left(1 + \gamma_b \frac{T}{P_{buckling}}\right)^{1/2} \tag{53}$$

Eq.(53) can be used in the numerical simulation to modify the eigenvalue ω_0 for the SDOF system of eq.(35)-(38).

3.3 SDOF for gravity loaded walls

For a gravity loaded wall simplified with the mass model as shown in left hand side of Fig.3, the work done by the blast load consists of both the deflection of the wall and the movement of the mass:

$$W = \int_0^L N(x)g(t)\phi(x)dx + m_0 g(\delta_0 - \delta_{axial}) \tag{54}$$

In this equation, m_0 is the mass on the top of the wall. In addition to the bending deflection, the work done by gravity from the movement of the mass should be considered.

According to the solution for the axial movement of the mass according to eq.(50), the total work will be determined as a function of the bending deflection w_0:

$$W = \begin{cases} p(t)w_0 LK_L & \text{after tension failure} \\ p(t)w_0 LK_L + \frac{m_0 g}{2L} K_A w_0^2 & \text{after crushing} \\ p(t)w_0 LK_L + m_0 g\left[\frac{1}{2L}K_A w_0^2 - \frac{2D}{d}|w_0|\left(1 - \frac{|w_0|}{2d}\right)\right] & \text{otherwise} \end{cases} \tag{55}$$

Consequently according to eq.(15), the equivalent load for SDOF becomes:

$$F_e(t) = \begin{cases} K_L P(t) & \text{after tension failure} \\ K_L P(t) + \frac{1}{2L} m_0 g K_A |w_0| & \text{after crushing} \\ K_L P(t) + m_0 g\left[\frac{K_A}{2L}|w_0| - \frac{2D}{d}\left(1 - \frac{|w_0|}{2d}\right)\right] & \text{otherwise} \end{cases} \tag{56}$$

According to the solution for the axial displacement of eq.(50), the solution for the kinetic energy of the wall with the top mass becomes:

$$K.E. = \frac{1}{2}\left[\frac{dw_0}{dt}\right]^2 K_M M + \begin{cases} 0 & \text{after tension failure} \\ \frac{1}{2} m_a \left[\frac{dw_0}{dt}\right]^2 \left(\frac{|w_0|}{L} K_A\right)^2 & \text{after crushing} \\ \frac{1}{2} m_a \left[\frac{dw_0}{dt}\right]^2 \left[\frac{2D}{d}\left[\left(1 - \frac{|w_0|}{d}\right)\right] - \frac{|w_0|}{L} K_A\right]^2 & \text{otherwise} \end{cases} \tag{57}$$

The equivalent mass (M_e) for the SDOF system will become:

$$M_e = K_M M + \begin{cases} 0 & \text{after tension failure} \\ m_0 \left(\frac{|w_0|}{L} K_A\right)^2 & \text{after crushing} \\ m_0 \left[\frac{2D}{d}\left[\left(1 - \frac{|w_0|}{d}\right)\right] - \frac{|w_0|}{L} K_A\right]^2 & \text{otherwise} \end{cases} \quad (58)$$

Again for small deformations, the strain energy for the wall is assumed to be dominant by bending according to eq.(11) and the equivalent stiffness will be the same as eq.(24).

4 Sectional quantities

A typical reinforced concrete wall consists of both the concrete and the reinforcement bars. A schematic is shown in Fig.5. In this figure, d is the thickness. The concrete is shown as the shaded section and the reinforcement bars are shown as solid dots. The reinforcement may be sized according to the expected loading condition of the wall. More rebars may be placed close to the surface that is expected to be subjected to the tension stress. In this figure, c_t is the covering distance on the tension side of the wall, and c_c is the covering distance on the compression side. In this figure, a is the distance from the compression surface to the rotation plane. This dimension is determined by the mechanical property of both the rebar and the concrete.

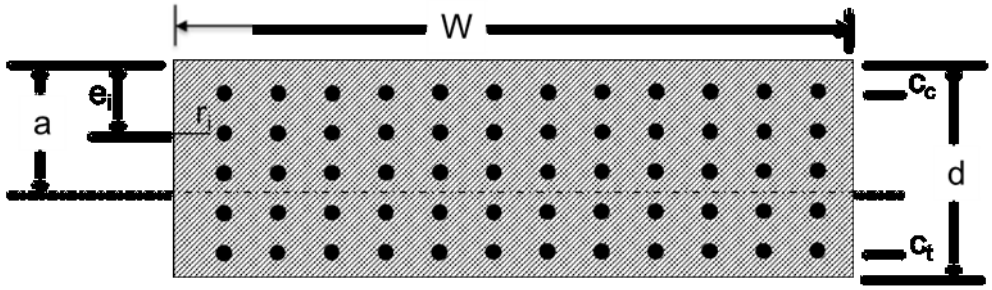

Figure 5: Schematic of a reinforced concrete wall cross section.

4.1 Area moment of inertia

The area moment of inertia with respect to the rotation plane should be determine to determine the bending resistance of a wall. For a reinforced concrete wall, the superposition method is considered.

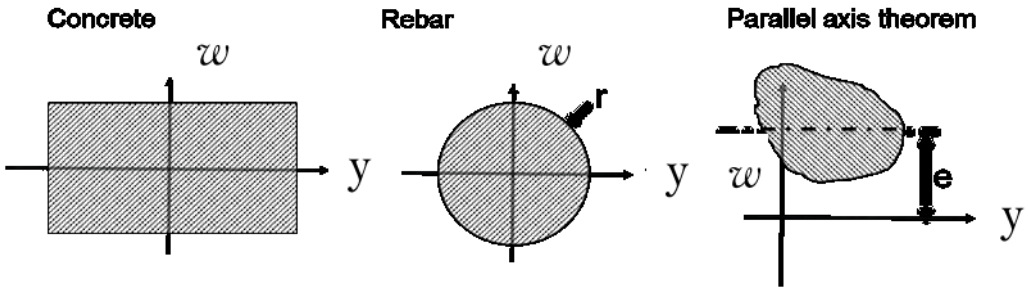

Figure 6: Basic geometry of the concrete and rebar.

To determine the moment of inertia for the wall section as shown in Fig.5, the basic geometry of the concrete and rebar for the wall as well as the parallel axis theorem are considered, see Fig.6. In this figure, w is the coordinate through the thickness, and y is the coordinate along the width of the wall. This results in a solution for the area moment of inertia with respect to the rotation axis a (Fig.5) to be:

$$I_a = \frac{Wd^3}{12} + Wd\left(a - \frac{d}{2}\right)^2 + \sum_{i=1}^{N} \pi r_i^2 \left[\frac{\pi r_i^2}{4} + (a - e_i)^2\right] \quad (59)$$

In this equation, N is the number of rebars. For each rebqar, r_i and e_i are the radius and its offset from the compression side of the wall surface, see the dimensions shown in Fig.5.

4.2 Equivalent elastic modulus

It is assumed that both rebars and the concrete will have the same strain under the bending load. The sectional forces will consist of the forces in the concrete and in rebars:

$$N_d = N_s + N_c \tag{60}$$

In this relation, N_d is the total axial load. N_s is the load on the rebar (steel), and N_c is the load on the concrete.

According to Hook's law, the equivalent Young's modulus E_e of the wall can be determined such as:

$$E_e = \frac{A_s E_s + A_c E_c}{Wd} \tag{61}$$

In this equation, A_s is the section area of the sum of the rebar, and A_c is the section area of the concrete.

4.3 Whitney's solution

The remaining quantity is the location of the rotation plane, as shown in Fig.5. According to the construction rule [16], the Whitney solution [33-34] is considered.

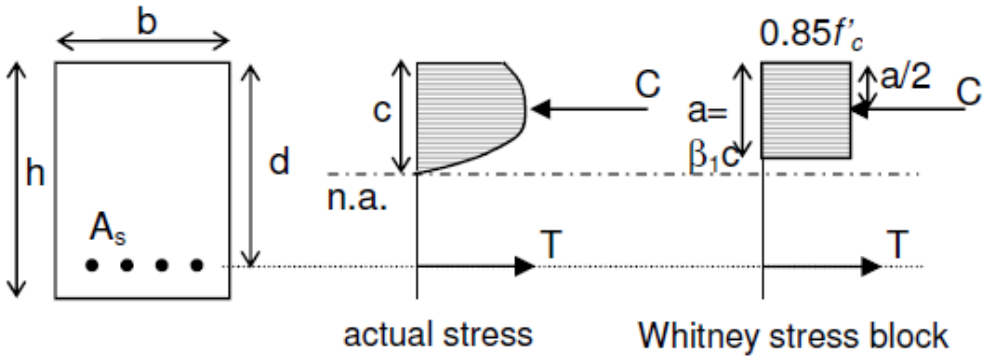

Figure 7: Schematic of the Whitney solution to determine the moment capability of a reinforced beam or wall section.

In the 1930s, Whitney [33] proposed a method for the use of a rectangular compressive stress distribution to approximate the bending capability of a reinforced wall. It was assumed that the concrete will not contribute to the tensile strength due to its low value compared to either the compression strength of the concrete or the tension strength of the rebar. The model is shown schematically in Fig.7.

According to this model, the compression capability C of the concrete is determined [16][32] according to an empirical approximation of:

$$C = 0.85abf_c \tag{62}$$

For which:

$$a = \beta_1 c \tag{62a}$$

$$\beta_1 = \begin{cases} 0.85, & f_c \leq 28\ \text{MPa} \\ max\left[0.85 - 0.05\left(\frac{f_c - 28}{6.9}\right), 0.65\right] & \text{otherwise} \end{cases} \tag{62b}$$

In these relations, c, as shown in Fig.7, is the effective section for the compression stress determined by the compression strength of the concrete.

The tensile capability of the reinforced wall is determined by the tension strength of rebar on the tensile part of wall. The tension strength is determined by:

$$T = A_{st}\sigma_y \tag{63}$$

In this relation, A_{st} is the area of rebars subjected to the tensile load and σ_y is the yield strength of the rebar.

To ensure that failure occurs when the tension strength of rebars and the compression strength of the concrete are simultaneously reached, it requires:

$$C\left(c - \frac{a}{2}\right) = T(d - c) \tag{64}$$

In this relation, $d = h - c_t$ is the effective depth of the rebar. Eq.(64) results in a condition:

$$0.85\beta_1 bf_c(1 - 0.5\beta_1)c^2 + A_{st}\sigma_y c - A_{st}\sigma_y d = 0 \tag{65}$$

Solution of this equation for the effective compression length results in:

$$c = \frac{-B \pm \sqrt{B^2 - 4AC'}}{2A} \tag{66}$$

In this solution:

$$A = 0.85\beta_1 W f_c(1 - 0.5\beta_1) \tag{66a}$$

$$B = A_{st}\sigma_y \tag{66b}$$

$$C' = -A_{st}\sigma_y(d - c_t) \tag{66c}$$

For a balanced solution when the rebar and concrete both reach their respective maximum capability, there will be a residual axial force. The axial force at the maximum bending capability will be determined according to:

$$N_d = C - T \tag{67}$$

This results in a solution for the axial load at the maximum bending capability of the reinforced wall:

$$N_d = 0.85\beta_1 cbf_c - A_{st}\sigma_y \tag{68}$$

By sizing the reinforcement bars according to$N_d = 0$, the optimal rebar will be determined according to:

$$A_{st} = \frac{0.85\beta_1 cbf_c}{\sigma_y} \tag{68a}$$

Note that c is a function of A_{st}, iterative solution is required for eq.(68a). The reinforcement determined by eq.(68a) will ensure the maximum bending capability is reached for a wall without the axial load.

5 Sectional capability

The sectional moment capability of a reinforced concrete wall is determined by both the strength of concrete and the strength of rebar. For a given wall, the maximum tension and compressive capability, and thus the maximum moment capability will be different depending on which parameter is strongest. They are determined by the construction of the wall. In the following sections, these strengths will be separately discussed.

5.1 Tension capability

The maximum sectional tension capacity of the wall with a constant section is determined by either the strength of the rebar or the strength of the concrete, whichever is strongest. The maximum tensile load that a wall can take is determined by:

$$(N_d)_{min} = -max(A_c f_t, A_s \sigma_y) \quad (69)$$

In this relation, $A_c f_t$ is the tension capability of the concrete, and $A_s \sigma_y$ is the tension capability of the rebar. They are determined by the strength of the material and their respective sectional area. In eq.(69), A_c and f_t are the sectional area and the tensile strength of the concrete. A_s and σ_y are the sectional area and tension strength of the rebar. The sectional tension capability will be determined by the maximum value of the tension capability of either the concrete or the rebar.

5.2 Compression capability

The maximum sectional compression capacity is determined by both the strength of the concrete and rebar:

$$(N_d)_{max} = A_c f_c + A_s \sigma_y \quad (70)$$

At compression, both the reinforcement and the concrete will contribute to the strength of the wall. In this equation:

A_c: is the concrete cross area $A_c = Wd - A_s$

A_s: is the rebar cross area

f_c: is the concrete compression strength

σ_y: is the rebar yield stress

5.3 Moment capability

The moment capability is determined by the Whitney's solution as given in 4.3. According to the solution, the maximum sectional bending capability is determined by:

$$M_d = A_{st} \sigma_y (d - c_t - c) \quad (71)$$

At the maximum sectional bending capability, there will be an axial load determined by eq.(68).

5.4 Euler's buckling limit

For a wall with a considerable height to thickness ratio, the buckling of the wall will limit its sectional load bearing capability. The buckling is determined by the condition when the work done by the axial load becomes larger than the strain energy of the wall due to deflection. At this condition, the wall loses its load bearing capability. The Euler's elastic buckling load is determined according to eq.(52).

5.5 Interaction diagram

The axial loaded wall will be subjected to both the bending moment due to the blast load and the axial load due to gravity and dynamic response of the mass above the wall. A simplified, but yet conservative, solution is to consider a general interaction diagram as shown in Fig.8, with straight interpolation between the limit load cases.

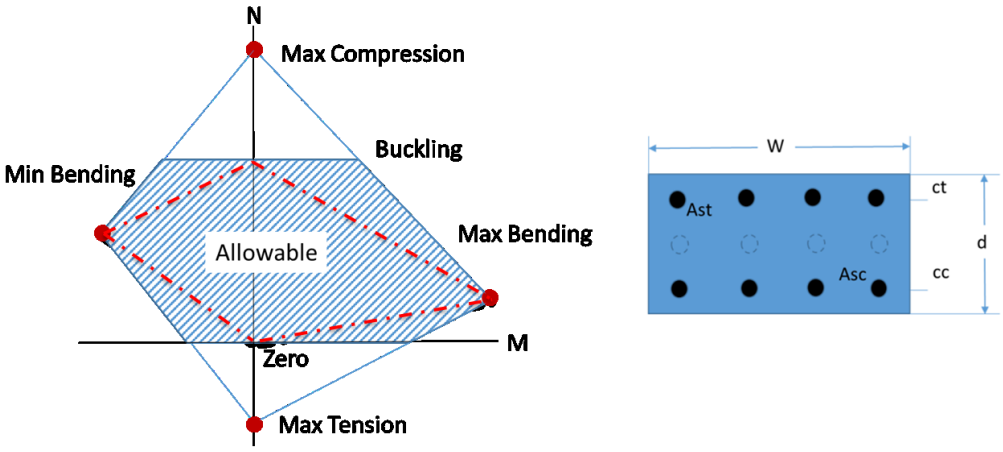

Figure 8: Interaction diagram for the axial loaded wall subjected to the blast loading condition.

In this diagram, the vertical axis is the axial load and the horizontal axis is the bending moment. The sectional capability of the wall is limited by the shaded area. This area is determined by tension, compression, as well as the moment capability of the wall. The buckling will put anoother limit on the sectional capability.

For a given wall, the maximum tension capability is given in eq.(69), the maximum compression capability is given in eq.(70). The balanced bending capability is determined by eq.(68) and eq.(71). Notice that the diagram may not be symmetric for the asymmetrically reinforced walls. The buckling load determined by eq.(52) may limit the compression capability of thin walls..

An even more conservative solution is shown in Fig.8 as the boundary limited by the dashed red lines. This solution is often found in the literature. It is however considered to be over-conservative even though it is simpler to apply the solution.

6 Failure criteria

The SDOF solution will not directly provide failure criteria for a wall under the blast loading condition. The failure should be considered according to the sectional capability of the wall. From the SDOF simulation, the deflection of the wall is estimated. From the deflection, the sectional moment is determined according to the beam theory. Together with the axial load determined by the gravity solution, the critical sectional moment will be determined by the interaction diagram as shown in Fig.8. The critical section will turn into a plastic hinge [23] when the sectional moment exceeds its capability. At the plastic hinge, the moment resistance will reach its maximum value and become constant.

Consequently, the deflection shape of the wall will change due to the forming of plastic hinge. Fig.9 shows an example of the basic assumption for the failure sequence of a wall with constrained supports. During the initial blast load for this case, the maximum moment due to the deflection will occur close to the support areas where there will have the maximum curvature. When the bending moment at either one of the locations exceeds the sectional moment capability, plastic deformation will occur to allow excessive deformation without significant increase in the rotational resistance.

The deflection shape will change from the fixed ends condition to the one with a single fixed end and a free rotation end, see the second figure from the left in Fig.9. For this deformation shape, the maximum bending moment will occur at the lower end of the support.

When the sectional capability at the lower support is also exceeded, the deflection shape will further change to a free support type as shown as the third picture from the left of Fig.9. For this simply supported wall, the maximum sectional moment will move to the center. When the sectional capability at the center of the wall is also exceeded, the third plastic hinge will be formed at the center of the wall. The deflection will then change to a free hinged form with only the plastic moment acting at the hinges to resist further bending of the wall.

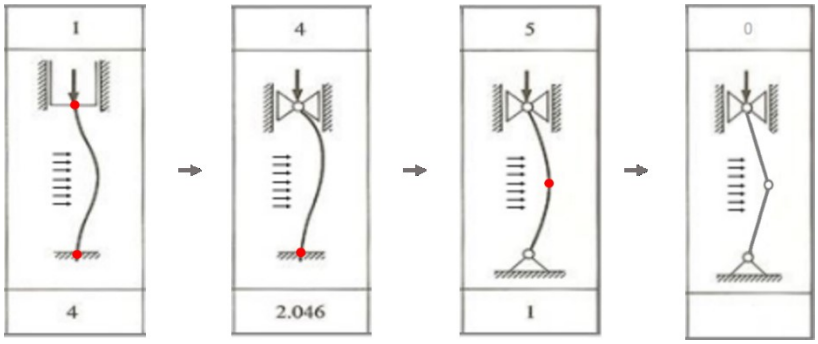

Figure 9: Schematic of the failure sequence of an axially loaded wall subjected to a blast load.

These failure patterns are related to the performance levels as defined by FEMA [35]. For example when one hinge has been formed, the structure will be classed as “Immediate Occupancy” (IO) level. When two hinges have been formed it is the “Life Safety” (LS) level. When three hinges have been formed, it is called the “Collapse Prevention” (CP) level. Other terms are also used to describe the damage extent. When all the plastic hinges are formed, it also called the “severe” damage, and when the first hinge is formed as shown in Fig.9, the damage may be named “minal”.

7 Shear Failure

So far, the solution is focused on the bending dominant failure. This is also the likely failure mode of relatively thin walls. For a blast load with high magnitude and very short duration, the acceleration in the middle of the wall may become excessive with resulting significant inertia resistance. The failure mode can change from bending dominant to shear dominant.

For a blast load with extreme amplitude, the reaction force at the supports of the wall may become high enough to create a local shear stress that exceeds the shear strength of the wall. As given in eq.(34), the reaction force is proportional to the magnitude of the pressure. When the shear stress exceeds the shear strength of the concrete, the wall may fail in a pure shear failure mode. The condition is determined by considering the average sectional shear stress according to:

$$\frac{V(t)}{Wd} \geq \gamma f_s \tag{72}$$

In this equation, f_s is the shear strength of the concrete and γ is a dynamic increasing factor, usually at a value of about $\gamma \approx 1.2$ for concrete. For walls, rebars are assumed not contributing to the shear strength of the wall.

A more complicated shear failure mode is the so-called flexural shear failure. This is the failure mode between the bending and pure shear failure. This mode occurs when the center part of the wall experiences significant acceleration and the inertia force due to such an acceleration may overcome the blast pressure and prevent further deflection at the center part of the wall. A schematic is shown in Fig.10. The deflection mode is illustrated on the right hand side of the figure. As a result, the maximum sectional bending moment will move away from the critical location (the center). In this case, the curvature in the center section may reduce when shear hinges may be created away from the center.

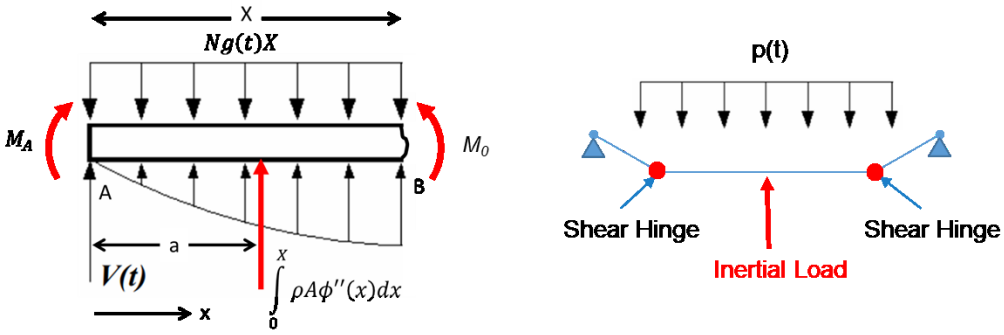

Figure 10: The schematic for the flexural shear failure mode.

The short moment arm, significant shear force, and axial load may lead to the failure to occur in the plane at some angle respective to the axis of the wall. Even though the failure mechanism may still be dominated by the bending moment, this failure phenomenon is often cited as the shear failure mode. Sometimes, it is cited as the flexural shear failure.

To study this failure mode, the loading condition on the shear section should be considered. The load on the shear section may be assumed according to the schematic as shown on the left hand side of Fig.10. In this case, the equilibrium of the moment with respect to the inertia force center requires:

$$V(t)a + M_A - M_0 - p(t)X\left(a - \frac{X}{2}\right) = 0 \quad (73)$$

In this equation, M_0 is the sectional moment capability at a distance X from the support. M_A is the sectional moment at the support. Unlike the solution as shown in Fig.2, X will be the shear arm of the wall between the support and the shear hinge.

To assume a linear deflection for the shear arm within the distance of X (the shear distance), a is solved according to eq.(33):

$$\frac{a}{X} = \frac{\int_0^1 f(x')x'dx'}{\int_0^1 f(x')dx'} = \frac{2}{3} \quad (74)$$

This gives a solution for the shear arm:

$$X = \sqrt{6(M_O - M_A)/p(t)} \quad (75)$$

This shear distance is different from that when the reaction force is determined according to eq.(31). The solution shows that the shear arm X will be independent of the length of the wall. It will be a function of pressure and the bending moment capability of the wall. When the amplitude of the pressure is high, the shear length will reduce and the likelihood of shear failure will increase. Eq.(75) shows that the higher the pressure, the shorter the shear arm may become.

For a simply supported wall, M_A will be zero while it may be assumed that $M_A = -M_O$ at the support when the rotation is constrained. Thus, the constraint of bending rotation at the support may increase the shear arm and move the shear failure location away towards the center.

For a flexural shear failure, the reaction force becomes:

$$V(t) = \sqrt{\frac{3}{2}(M_O - M_A)p(t)} \quad (76)$$

This is a function of both the peak pressure and the moment capability of the wall.

8 Validations

For the validation of SDOF solution for a gravity-loaded wall, two test series have been considered. The first test series, Test Series 1, is performed in 2017 [14]. The second series, Test Series 2, is performed in 2020 [15].

The basic setups are similar for both tests. The schematic of the experiments is shown in Fig.11. For these tests, a ½ scaled wall element is used for the test object due to the dimensional limitation of the shock wave tube used for the tests. Fig.11 shows the dimensions of the test object and the placement of various sensors.

The axial load is applied on the top of the test objects to simulate the gravity load. Due to the facility limitation, hydraulic actuator is used to apply the axial load. When the desired load level is achieved, the valve of the hydraulic actuator is closed to prevent movement of the actuator during the blast test. This is a less ideal solution to simulate the gravity load since the deformation of the test rig is difficult to determine.

The deflection of the test object is recorded at three locations as shown in Fig.11 with laser displacement sensors at D1-D4. The force from the actuator is recorded with a load cell on the hydraulic cylinder during the blast test to monitor changes in the axial load. The rotation of the test object is constrained at the upper end with slide rollers as shown in Fig.11. The rollers prevent the rotation while allowing the axial movement at the top of the wall.

In addition to the blast tests, quasi-static bending tests were also performed to determine the bending capability of the wall when subjected to different axial loads. The test setup is shown on the right hand side of Fig.11. For the quasi-static bending test, the transverse load was applied by a hydraulic actuator on the side of the test objects, see the right hand side of Fig.11. Three-point quasi-static bending tests were performed for Test Series 1, and four-point bending tests were performed for Test Series 2.

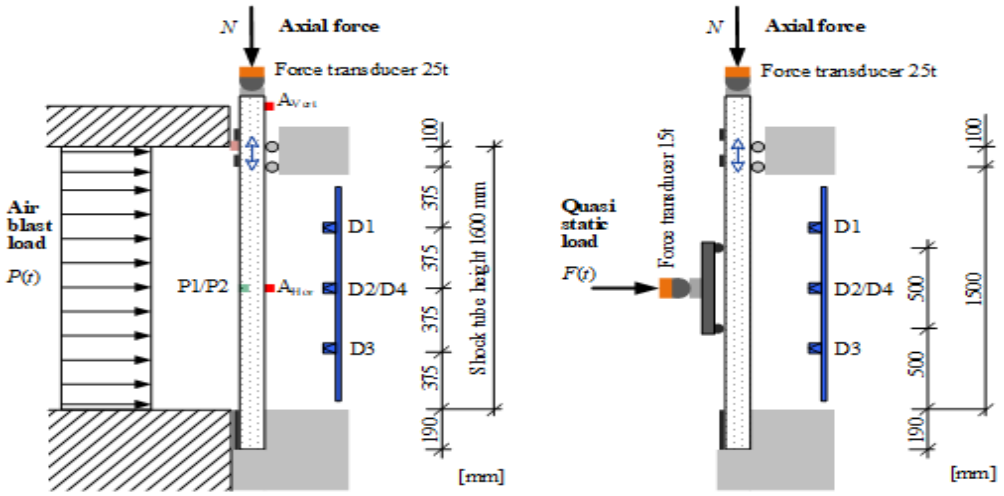

Figure 11: Schematic of the setups for the validation tests for the blast and quasi-static load.

The test objects were manufactured with scaled rebars (6 mm) and aggregate (8 mm). Fig. 12 shows the sectional dimensions and the reinforcement arrangement. To ensure consistency in the material data for the concrete, both cube and cylinder standard concrete specimens were made for the concrete mixture used for the test objects. Compression and

splitting tests were made with these specimens in coordination with the blast and quasi-static test scheme to determine the mechanical property of the concrete at the test moments. The detailed reports of the tests are provided in [14-15].

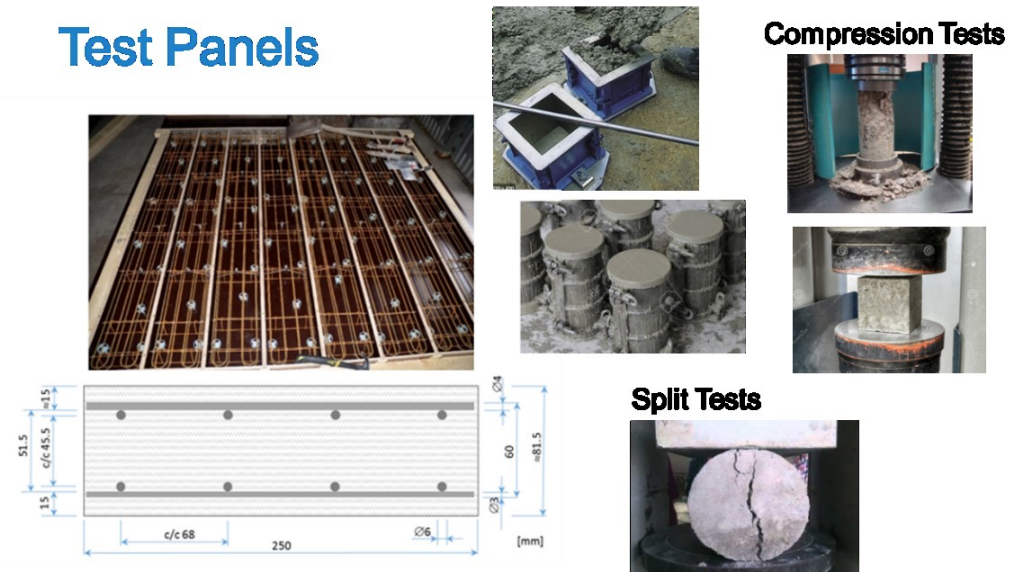

Figure 12: The test object dimensions and reinforcement, together with the cube and cylinder specimens for the compression and splitting tests of the concrete for the test series.

8.1 Quasi-static tests

The quasi-static tests are used to determine the non-linear stiffness and bending capability of the test objects. They are sometimes used to determine the nonlinear resistance of a structure against the applied load for SDOF simulations.

According to eq.(27-28) and eq.(56), the resistance of the wall subjected to a gravity load is determined according to:

$$P(w_0) = \frac{1}{K_L}\left[K_K \frac{EI}{L^3} - m_0 g \left(\frac{D}{d^2} + \frac{K_A}{2L}\right)\right] w_0 + \frac{2D}{K_L d} m_0 g = R(w_0) + R_0 \qquad (77)$$

In this equation, $R(w_0) + R_0$ is considered to be the resistance of the wall against the bending load. It is sometimes used directly in the SDOF solution to replace the equivalent solution. It is sometimes considered to be a better representation of the resistance of a specific wall against the transverse load.

It is shown in eq.(77) that the resistance will be dependent on the patterns of deflection for an applied load. For example, the results from a three-point bending load will differ from the experimental results from a four-point bending load. The axial gravity load will affect the stiffness of the resistance.

An example of the analytical model is given in Fig.13 for the analytical resistance of a beam subjected to a quasi-static transverse load. It is shown that the forming of plastic hinges near the support will change the stiffness of the beam from a fixed end condition to a free rotationcondition. When a plastic hinge is formed, these hinges will provide nearly constant resistance to rotation. The resistance of the beam will be determined by the

sectional capability as well as the patterns of deflection due to different boundary constraints.

Two solutions may be assumed, one is based on the constant moment on the hinge. The solution is shown in Fig.13 as the gray lines. Another one is based on the accumulation of the bending moment as shown in Fig.13 as the blue lines. The accumulation of the bending capability will result in higher bending resistance.

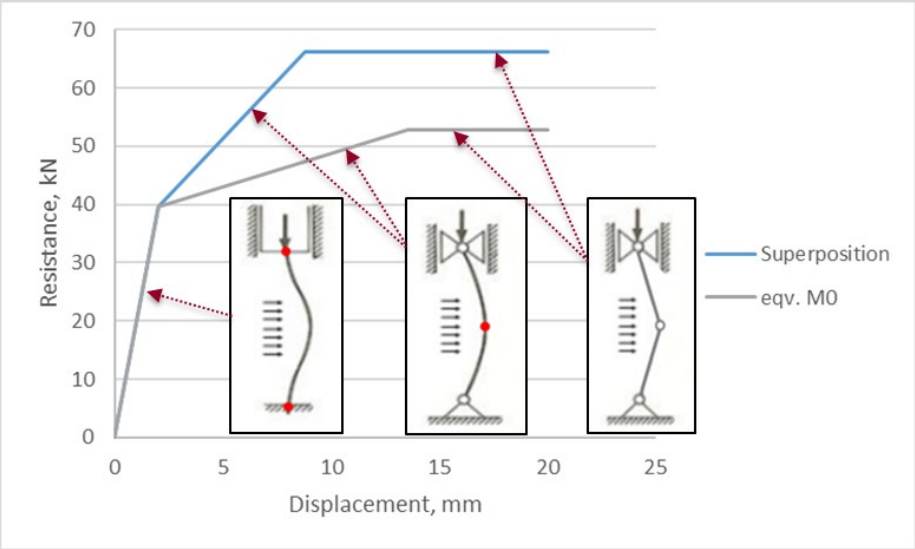

Figure 13: Example of the analytical solution for the resistance of test objects.

Two different sets of quasi-static tests have been performed in [14] and [15]. The three-point bending tests are performed in [14] while four-point bending tests are performed in [15]. The similar case for both test series is for the axial load of 80 kN. For both test series, the reinforcement is according to the same specification, but the measured compression strengths of the test objects are different. For Test Series 1, the cube compression strength is around 45MPa while for Test Series 2, 20MPa.

The comparison of the transverse resistance as a function of the deflection at the center of the wall is shown in Fig.14. In this figure, the dashed red curve is the results from Test Series 1 for three-point bending load and the solid blue curve is from Test Series 2 for four-point bending load. The results indicate that four-point bending will give significantly higher resistance eventhough the concrete has a lower compression strength. The initial stiffness is also higher for four-point bending, compared to that for three-point bending.

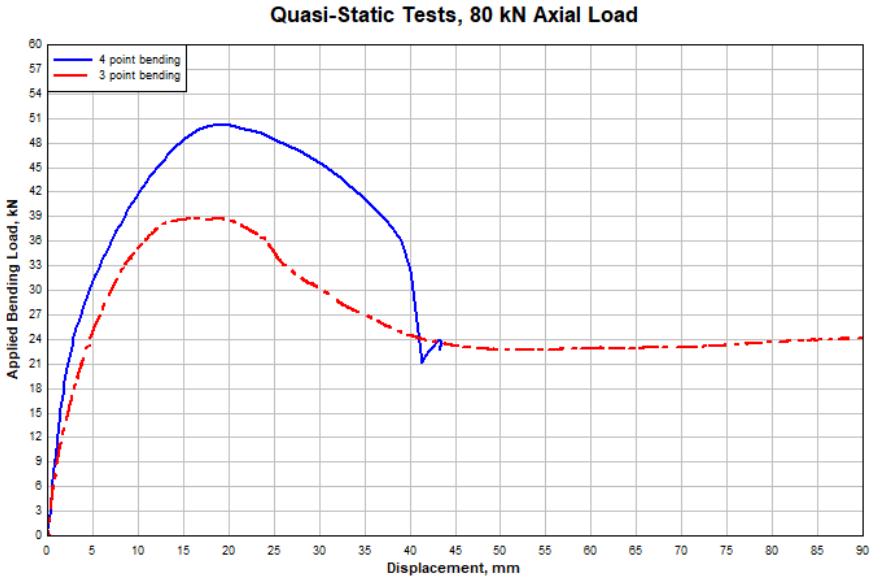

Figure 14: Comparison of the wall resistance against quasi-static transverse load as a function of the deflection between Test Series 1 and Test Series 2 for three-point bending as the red curve and four-point bending as the blue curve.

Part of the reason for the difference in the measured resistances is due to the difference in the patterns of deflection between the test setups. Different load setups will result in different maximum moment in the beam for a given deflection. The resistance to a transverse load for the fixed end wall as a function of either the maximum moment or the maximum transverse deflection is deterimined by:

$$P_{fixed-end} = \begin{cases} \frac{12M_{max}}{L} = 384\frac{EI}{L^3}w_0 & \text{uniform pressure} \\ \frac{8M_{max}}{L} = 192\frac{EI}{L^3}w_0 & \text{three} - \text{point bending} \\ \frac{18M_{max}}{L} = 259.2\frac{EI}{L^3}w_0 & \text{four} - \text{point bending} \end{cases} \quad (78)$$

The solution shows that the transverse stiffness of the wall will become larger and the bending moment will be lower for four-point bending. When the rotation is allowed at the ends, the resistance of the wall is determined by:

$$P_{free-end} = \begin{cases} \frac{8M_{max}}{L} = 76.8\frac{EI}{L^3}w_0 & \text{uniform pressure} \\ \frac{4M_{max}}{L} = 48\frac{EI}{L^3}w_0 & \text{three} - \text{point bending} \\ \frac{6M_{max}}{L} = 56.35\frac{EI}{L^3}w_0 & \text{four} - \text{point bending} \end{cases} \quad (79)$$

For a uniform pressure, the quasi-static resistance has to be scaled so that the stress state at the critical locations will become comparable. The experimental result from three-point bending tests has to be scaled by a factor of 1.5 for the resistance, and a scale factor of 0.5 should be applied for the deflection. For the experimental results from four-point bending tests, the magnitude of resistance has to be scaled by a factor of 0.67, and the deflection has to be scaled with a factor of 0.675.

After the plastic hinges are created near the supports, the deflection pattern of the wall will change from the fixed end condition to the free end condition and the experimental resistance has to be scaled according to eq.(79).

For the experimental results from three-point bending tests, the magnitude of the resistance has to be scaled by a factor of 2, and the resistance from four-point bending tests has to be scaled by a factor of 1.33. The experimental deflection has to be scaled by a factor of 0.625 for the results from three-point bending tests, and a factor of 0.734 for the results from four-point bending tests.

The comparison of the resulting equivalent resistance for the uniform pressure is shown in Fig.15. Compared to the original resistance results as shown in Fig.14, the equivalence resistance from Test Series 1 becomes now slightly higher than that from Test Series 2. This is a different trend than that shown in Fig.14 where the resistance from Test Series 2 appeared to be higher than those from Test Series 1.

There is an excellent agreement in the elastic deformation range for the equivalent resistance between Test Series 1 and Test Series 2. The results begin to differ when yield occurs. As mentioned previously, the measured strength for the concrete in Test Series 1 is higher than that in Test Series 2. The resistance of Test Series 1 should thus be higher than that for Test Series 2. This is the trend revealed in the comparison as shown in Fig.15 for the equivalent resistance. Test Series 1 indicates higher resistance and a slightly less ductility compared to those from Test Series 2 as shown in Fig.15.

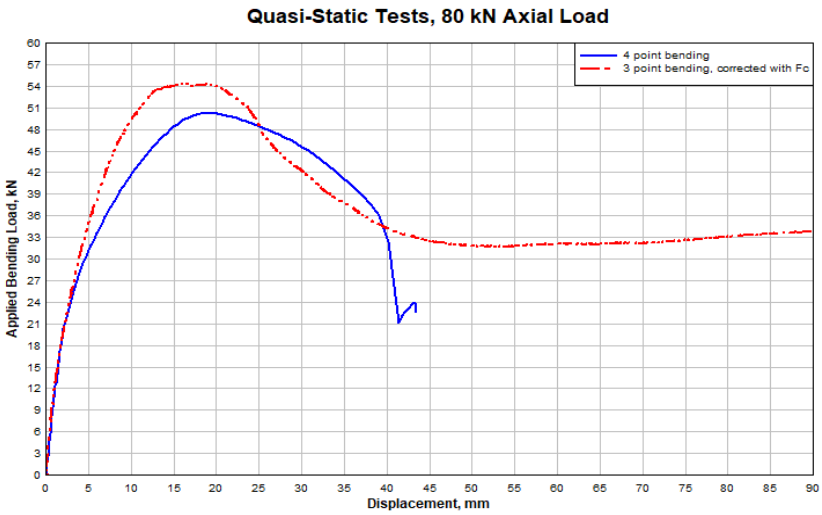

Figure 15: The equivalent resistance from the quasi-static tests for a uniform transverse pressure.

Based on the measured properties of the concrete and rebar, the analytical resistance of the test objects is determined. It is shown that the accumulation solution (superposition as shown in Fig.13) is a better presentation of the bending resistance of the wall. The comparison of the analytical and experimental bending resistance is shown on the left hand side of Fig.16. In this figure, the equivalent bending load as a function of the maximum deflection of the wall is compared. The comparison shows a reasonable agreement between the analytical solution and the experimental results when the wall is subjected to the axial load.

When there is no axial load applied on the test objects, the initial bending stiffness from the measurements shows to be significantly weaker than the analytical one, see the comparison between the dashed blue lines for the analytical solution and the green curves from the experiments.

The quasi-static bending tests were performed at the same rig as those for the blast tests with the test objects placing at the standing position. There were no pretension to close gaps in the contact areas between the test objects and the rig. It was shown that there is a significant movement of the hydraulic actuator before full contact were established between all the contact areas. These will artificially lead to excess transversal displacement (lower stiffeness) in the measurement.

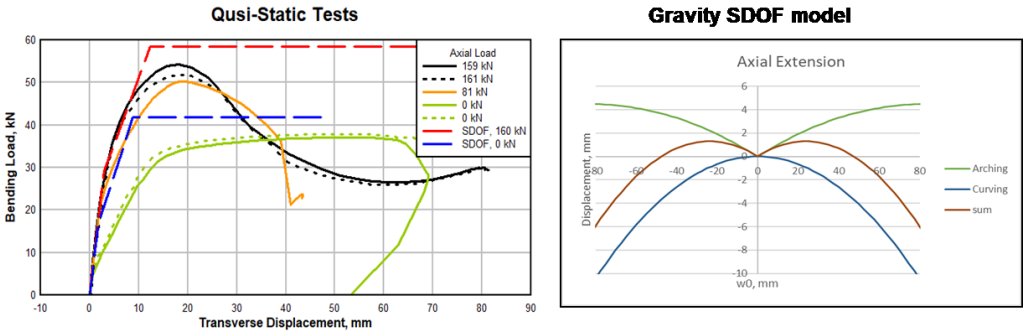

Figure 16: Comparison of the analytical resistance with the equivalent resistance from the tests for different axial loading condition.

The key element in the SDOF solution is for the approximation of the axial displacement when the arching effect is involved. The analytical solution of the axial displacement is shown on the right hand side of Fig.16 for the test object. In this figure, the blue curve is for the displacement due to bending deflection and the green curve is the deflection due to rigid rotation. The bending of the beam will lead to a downward movement of the mass and reduce the axial load which is not what is observed in the experiments.

The rigid rotation will lengthen the wall as shown at the green curve on the right hand side of Fig.16. This action will push the actuator to increase the axial load. The maximum extension due to the rigid arching effect will occur at the bending deflection of about 80 mm, near the whole thickness of the test object.

The experiments showed that the maximum axial load occurred at the deflection distance between 10 and 30 mm, see the result shown on the left hand side of Fig.16. The combined flexural displacement and the rigid arching according to the solution of eq.(50) is shown on the right hand side of Fig.16 as the brown curve. The analytical solution for the axial displacement will have the maximum axial extension at a value of around 20 mm. This is a confirmation that assumptions made for the solution of the axial displacement are reasonable.

8.2 Dynamic tests

The blast tests were performed in a shock tube schematically shown in Fig. 17. For the blast tests, an explosive charges were suspended at the center of the tube at various distance, see the left hand side of Fig.17. Use of the shock tube will create a reasonable uniform blast pressure on the test objects. The placement of the test object is shown on the right hand side of Fig.17. In this picture, the light-gray part is the test object. A steel frame is used around the test object to stiffen the rig. Gaps between various components are sealed to prevent the leakage of air to the back side of the test object. Two reusable pressure gauges are placed on the steel frame on both side of the test object at the center section to record the blast overpressure during the tests.

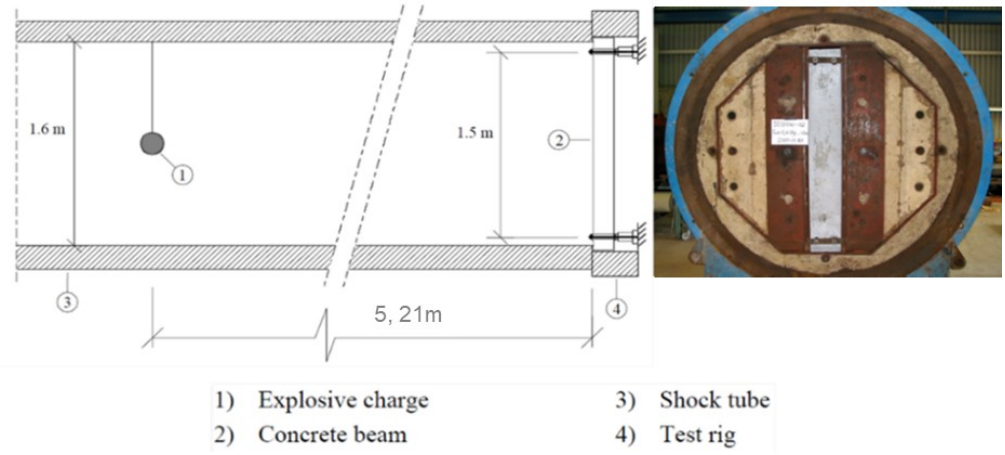

Figure 17: Experimental setup for the blast loading tests in the shock tube for the scaled wall elements.

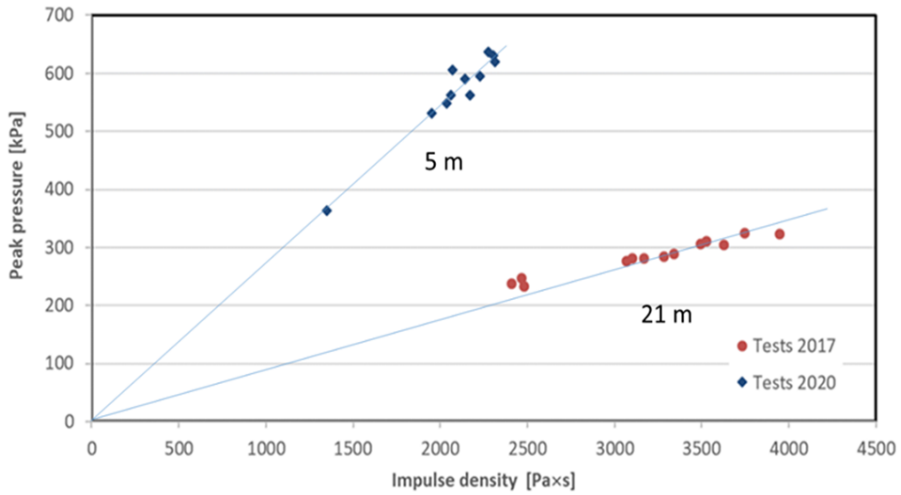

Figure 18: The range of blast load for Test Series 1 for a standoff distance of 21 m and Test Series 2 for a standoff distance of 5 m.

By changing the charge size and distance from the test object, blast load with various characteristics were created. A comparison of the peak pressure as a function of the impulse density is shown in Fig.18 for Test Series 1 and 2. It is shown that an increase in the charge mass will increase both the peak pressure and impulse density, while change in the standoff distance between the charge and the test object will change the slope of the peak pressure with respect to the impulse density. Longer standoff distance between the test object and the charge will generate stronger impulse at the comparable peak pressure level. Shorter standoff distance generates higher pressure for a given impulse density.

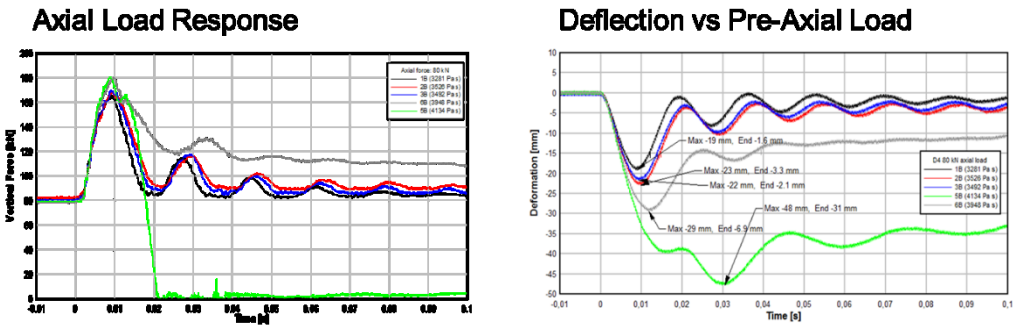

Figure 19: Example of the measurement of dynamic axial load, on the left hand side, and the maximum deflection, on the right hand side.

Examples of the recorded axial load and bending deflection as a function of time are shown in Fig.19 for the axial load, on the left hand side, and bending deflection, on the right hand side. These measurements are used to validate the SDOF solution.

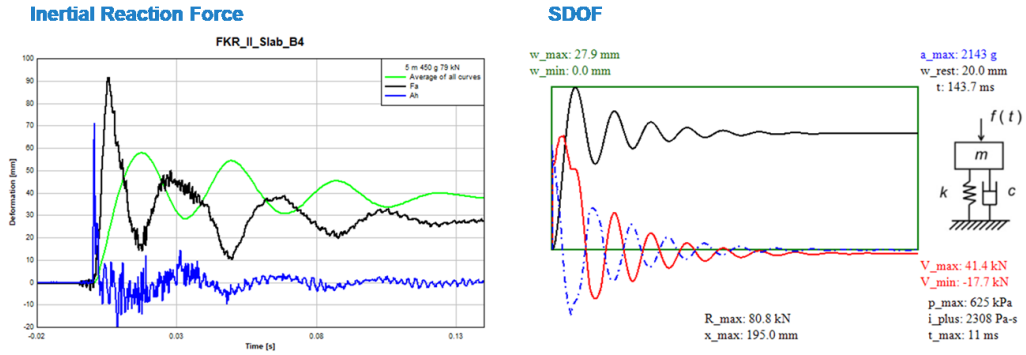

Figure 20: Estimation of the damping coefficient based on the simulations and the experimental results.

The first use of the experimental result for SDOF solution is to determine the damping coefficient. There is no analytical solution for this coefficient. It is however possible to estimate the value according to the experimental results.

By considering the number of periods of the response that occur when the dynamic deflection became fully damped out, the damping coefficient for SDOF can be estimated. Fig.20 shows a comparison between the experimental measurement of the deflection and the SDOF results. It is shown that a damping coefficient of about 5 percent will result in a reasonable agreement with the measurements. In this figure, the left hand side is the measurement of the bending deflection shown as the green curve, the bending acceleration, shown as the blue curve, and the axial load, shown as the black curve.

The simulations according to SDOF model is shown on the right hand side of Fig.20. In this figure, the black curve is the bending deflection, the red curve is the reaction force on the support, and the blue curve is the bending acceleration.

In addition to the experiments, finite element analysis (FEA) based on [20] is performed for several test conditions according to [15]. Three experiments are chosen for the zero, 79 kN, and 164 kN axial preload. These three cases are chosen since the level of blast load leads to the need to include the shear failure mechanism in the SDOF solution. The recorded blast profile is shown in Fig.21, which will be used as input for both FEA

simulations and SDOF analyses. In all the following analyses, the concrete is assumed to be in the quality of C20.

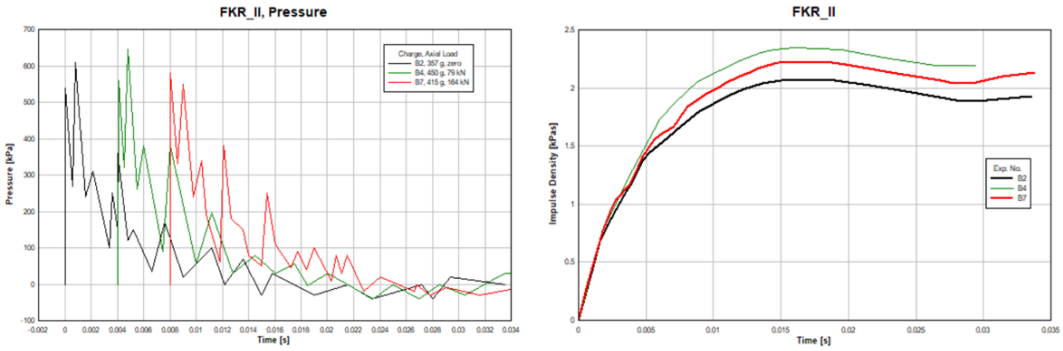

Figure 21: The recorded blast profile of the test on the left, and the impulse density on the right.[15]

8.2.1 Test B2

The object B2 is tested for a charge mass of 357 g without the axial preload. The comparison of post damage pattern between FEA and the test is shown in Fig.22. Both the test and the simulation shows multiple crackings in the center section as well as the near support areas. The simulation shows a reasonably good agreement with the test result.

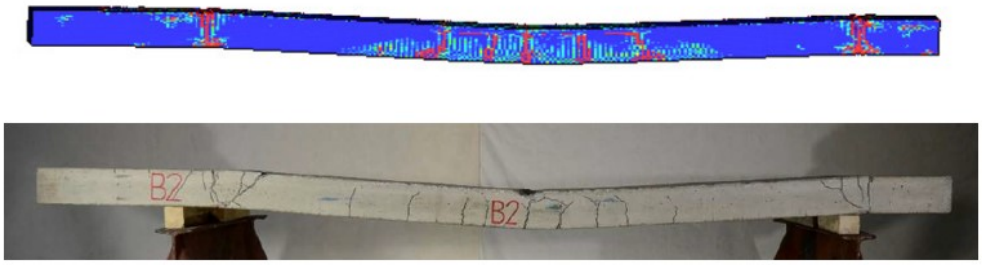

Figure 22: Comparison of the cracking patterns between the simulation and the experiment for the test object B2 for a charge mass of 357 g placed at a distance of 5 m from the surface of the test object. This test is performed without axial preload [15].

The comparison of the maximum deflection at the center of the specimen is shown in Fig.23. In this figure, the green curve is the experimental recording and the red curve is the FEA result. The comparison shows that the period of response has a good agreement between FEA and experimental results. The simulation gives a lower deflection, compared to that from the experiment. The damping of the response from the simulation is also stronger.

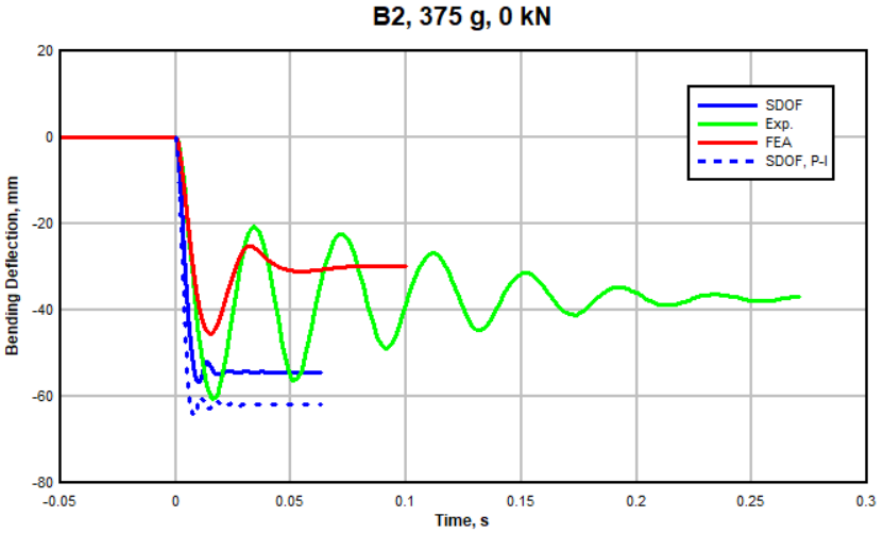

Figure 23: Comparison of the maximum deflections for Test B2 without axial preload. In this figure, the green is from experiments, red from FEA, and blues from SDOF.

The deflection from SDOF simulation is shown in Fig.23 as the blue solid curve. It is shown that the SDOF results in a maximum deflection closer to the test result, compared to that from FEA. Both the response period and the time to maximum deflection from SDOF is much shorter. This may be due to that SDOF solution is based on the elastic perfectly-plastic assumption. In the SDOF solution, the material will not have the intermediate elastic-plastic deformation regime which may become significant for the concrete and rebar.

SDOF solution is based on the energy balance constraint. The work done by the blast load will totally consumed by the plastic deformation which is determined by the maximum deflection. The SDOF solution seems to be adequate to capture the maximum deflection. In Fig.23, a SDOF result for a simplified triangle pressure profile is also presented as the dashed blue curve. It is shown that by idealizing the blast load as a triangle profile with corresponding peak pressure and impulse density, the deflection will become slightly higher.

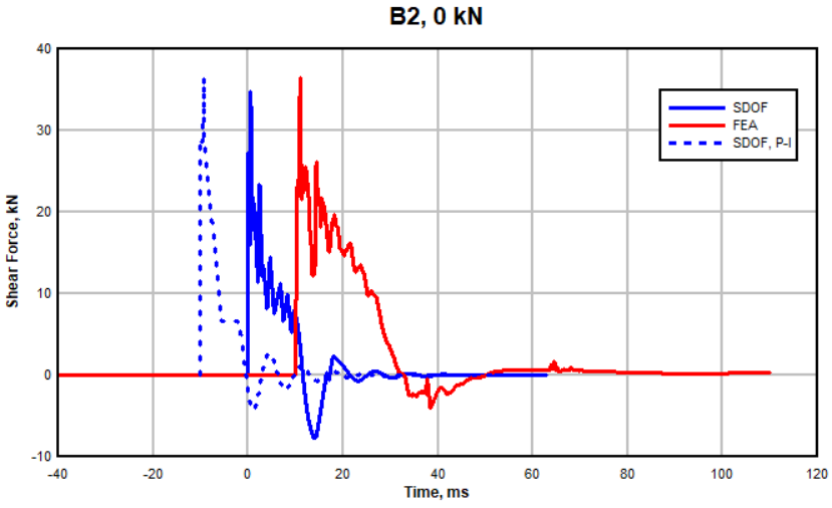

Figure 24: Comparison of the reaction force for Test B2 at the top support. The time axis is shifted on purpose to improve the visual comparison.

The reaction force is a major concern when complex failure is considered. It will affect shear failure pattern near the support. It is essential to verify that the solution as given in Section 2.3 is reasonable. For this purpose, the reaction force from FEA is compared to that from SDOF solution. For Test B2, the comparison is shown in Fig. 24. In this figure, the red curve is the FEA result and the blue curves are SDOF results. It is shown that the maximum shear forces are in a reasonable agreement between FEA analysis and SDOF solution even when the blast is simplied as a simple triangle form (shown in the figure as the dashed curve). This gives confidence using the SDOF solution as a shear failure criterion.

8.2.2 Test B4

An axial preload is applied for Test B4 at 79 kN. The comparison of the post cracking pattern between FEA and experiment is shown in Fig.25. It is shown that when a large axial preload is applied to the specimen, crack will become more concentrated to the critical locations of the center and the supporing areas. There is an observable spall area in the compression surface of the specimen, instead of longitudinal cracking as observed for the specimen without axial preload, see Fig.22.

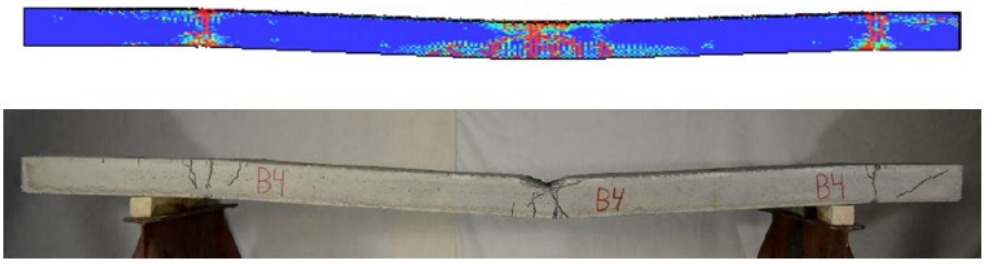

Figure 25: Comparison of the patterns of cracking between the simulation and experiment for Test B4 for a charge mass of 450 g placed at a distance of 5 m from the surface of the test object. This test is performed with an axial preload of 79 kN [15].

The comparison of the maximum deflections for B4 is shown in Fig.26, again with the test recording as the green curve, FEA as red, and SDOFs as blue. The test still shows larger deflection, compared to that from FEA, indicating the need for improvement in FEA simulation. It should be mentioned that the axial load is applied to the specimen in a different way for the test and FEA simulations. As mentioned in [20], the axial load is applied to the specimen with a hydraulic actuator in the test while in FEA, the gravity load is applied instead. There will be difference when the dynamic inertial force of the mass is considered.

The SDOF gives smaller deflection than that of FEA as the blue curves in Fig.25 show. This may be due to the difference when the axial load is applied. For FEA and SDOF solution, even though the load is applied as an equivalent mass on top of the test object, there is a contact solution for FEA simuluation which will not allow tension force between the mass and the specimen. For SDOF solution, the mass is permanently connected to the specimen. This may reduce the bending deflection in the solution. Again to simplify the blast load as a triangle form will slightly increase the maximum deflection as shown in the figure as the dashed blue curve.

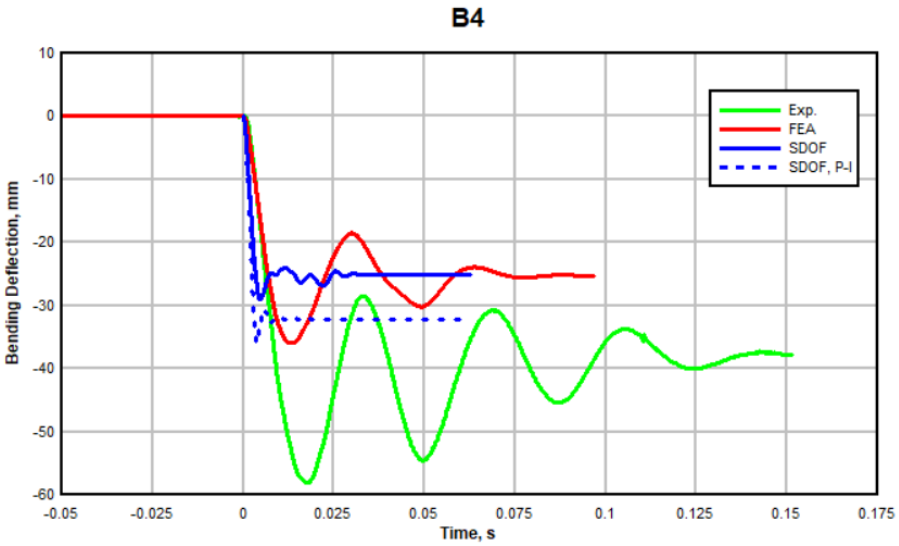

Figure 26: Comparison of the maximum deflections for Test B4 with an axial preload of 79 kN. In this figure, the green is from experiments, red from FEA, and blues from SDOF.

When the axial load is applied, it is a concern how it may affect the solution for reaction forces from SDOF. A comparision is shown in Fig.27 for the reaction force at the top support of the specimen. This comparison shows that SDOF solutions till give a reasonable top shear force, compared to that from FEA simulation.

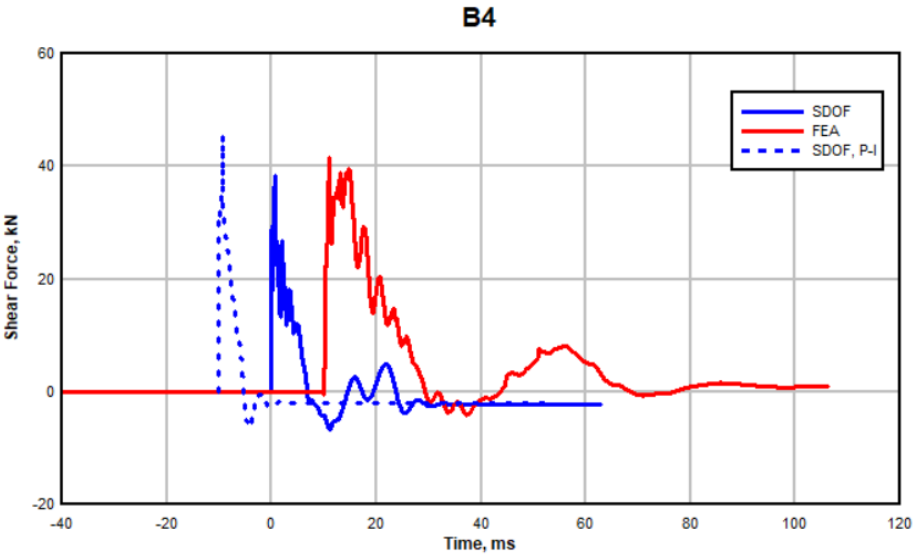

Figure 27: Comparison of the reaction force for B4 at the top support. The time axis is shifted on purpose to improve the visual comparison.

For the SDOF solution, the critical assumption is for the axial movement included in Eq.(48-49). The axial movement will determine the dynamic axial force applied on the wall due to both the gravity and the inertial force during the blast load. Since the magnitude of the axial movement is very small, the displacement measurement during the test is not reasonably accurate. To compare to the result from FEA is an option to determine whether or not the assumption is reasonable.

For Test B4, the comparison between the displacement between FEA and SDOF solution as a function of the bending deflection is shown in Fig.28. In this figure, the blue curve is the SDOF result, and the red curve is the FEA result.

The dynamic axial movement from FEA and SDOF is different. The FEA simulation shows that the maximum axial movement occur not at the maximum bending deflection (the horizontal axis), but during the springback phase of the wall at at value of about three fourth of the maximum deflection, see the red curve.

The solution from SDOF is different. The axial movement is in proportion to the bending deflection. This is due to the shape function assumed for SDOF solution. However, since the maximum axial load will be related to the maximum axial movement, it is important that the maximum value will be in agreement between FEA and SDOF result. The comparison in Fig.28 shows that both solutions give comparable maxium axial displacement, eventhough the behavior is completely different. Notice that the axial displacement is less than 1 mm, for a wall length of 1500 mm.

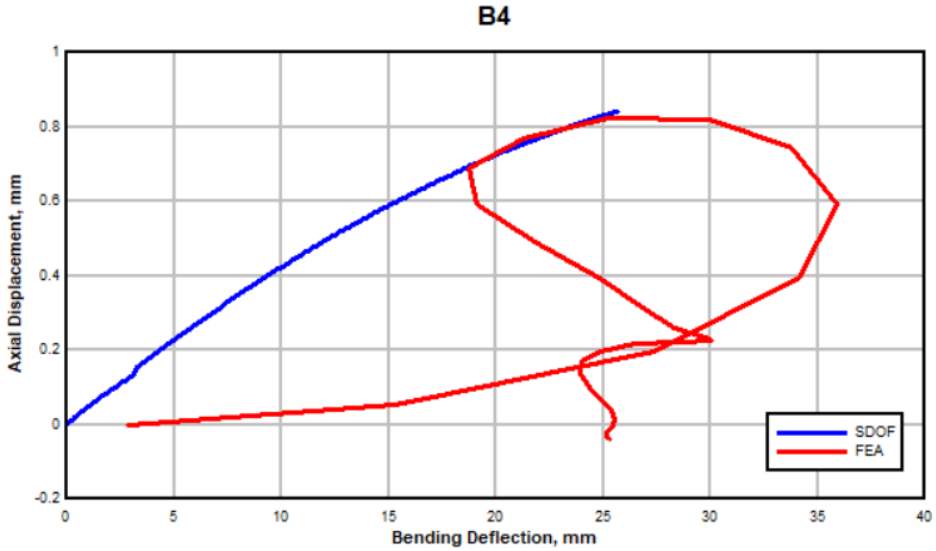

Figure 28: Comparison of FEA and SDOF result for the axial displacement as a function of the bending deflection for B4 test.

The comparison of the axial load is shown in Fig.29 for the result from the test and the analyses. In this figure, the test result is shown as the black curve. The result from FEA is shown as the red dashed curve, and the result from SDOF is shown as the blue dashed curve.

The axial loads from the test, FEA, and SDOF are not directly comparable due to the difference in the ways that the axial load is applied. During the blast event, the dynamic characteristics of both the rig and hydraulic system will affect the response of the experimental axial load. The FEA uses a mass on top of the specimen with contact conditions which will not allow tension between the mass and the specimen. For SDOF solution, the mass is rigidly connected to the specimen.

For Test B4, it is shown that FEA gives the highest axial load while the load estimated from SDOF agrees better with the test result. Again due to the elastic perfectly-plastic assumption in SDOF solution, the duration of the axial load is much shorter.

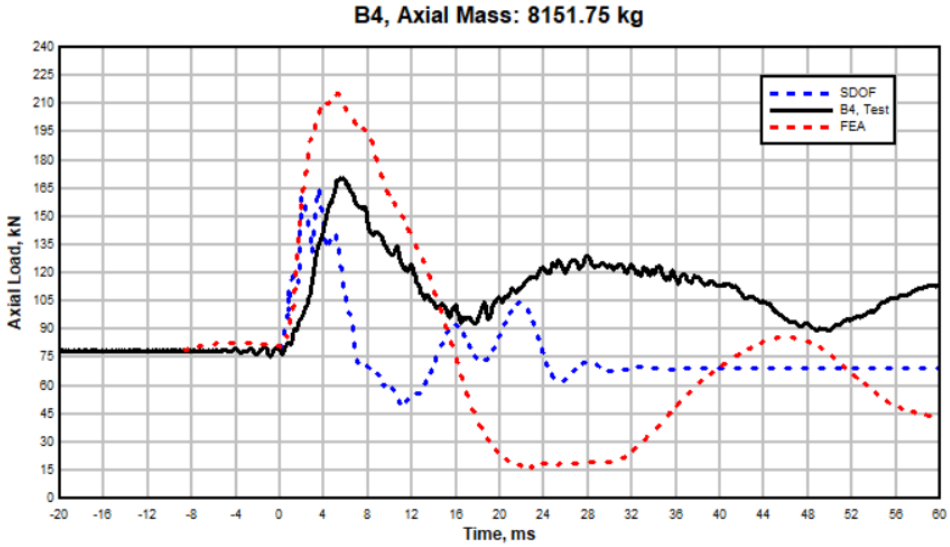

Figure 29: Comparison of the axial load between the test and analyses.

8.2.3 Test B7

Test B7 is performed with a very high axial load, at a level of 164 kN. At this load level, the initial axial compression stress is at 8 MPa, nearly half of the compression strength of the concete [15]. The comparison of the post cracking patterns between FEA and the test is shown in Fig.30. Again, the cracking pattern follows the trend as shown for Test B4 for the localization of the cracking near the critical locations. From both the simulation and test, there appears a large spall damage in the center on the blast side.

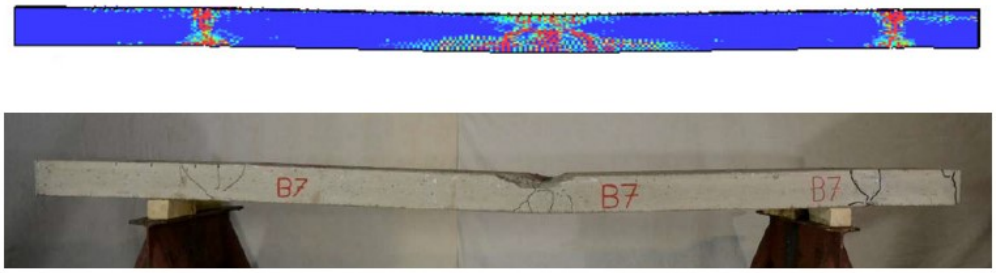

Figure 30: Comparison of the cracking patterns between the simulation and the experiment for the test object B7 for a charge mass of 415 g placed at a distance of 5 m from the test object. This test is performed with an axial preload of 164 kN [15].

The comparion of the maximum bending deflection is shown in Fig.31 with the test result as the green curve. The FEA result is shown as the red curve and the SDOF results are shown as blue curves. Again, FEA simulation results in a significantly lower deflection. The SDOF results are between FEA and test results. The FEA has the lowest residual deflection and SDOF has the highest residual deflection. The test result the residual deflection is in between. The result from FEA still shows significant damping. This can be a focus area in the future effort for FEA simulations.

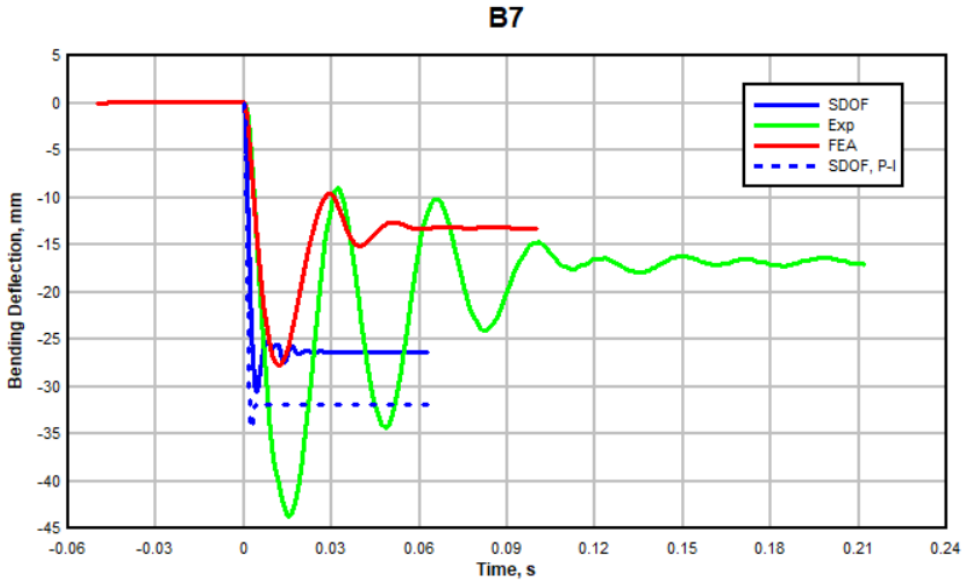

Figure 31: Comparison of the deflections for Test B7 with an axial preload of 164 kN. In this figure, the green is for experiments, red for FEA, and blues for SDOF.

The agreement in deflection between FEA and SDOF is reasonable for the maximum value, but there will be a large difference in the residual deflection. As mentioned previously, SDOF is based on the elastic perfectly-plastic assumption. Ignoring the non-linear elastic-plastic response in the concrete and rebar will prevent the springback of the beam. Simplification of the blast load as a triangle load will, as for B4, result in a larger deflection which may give a conservative result.

The comparison of the reaction forces at the top support is shown in Fig.32 for B7 test. In this case, SDOF results in slightly lower values..

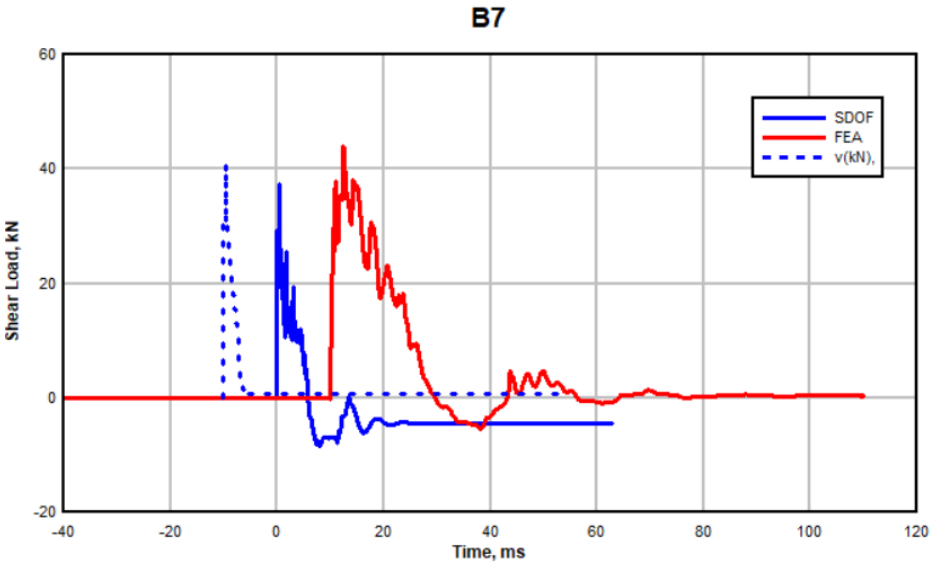

Figure 32: Comparison of the reaction force for B7 at the top support. The time axis is shifted on purpose to improve the visual comparison.

The comparison of the axial load between the test and the analyses is shown in Fig.33. In this case, SDOF gives higher axial load. The test and FEA have similar top load, but

differs greatly in the rebound phase. The simulation seems to have much lower axial load after the top value, compared to the test result.

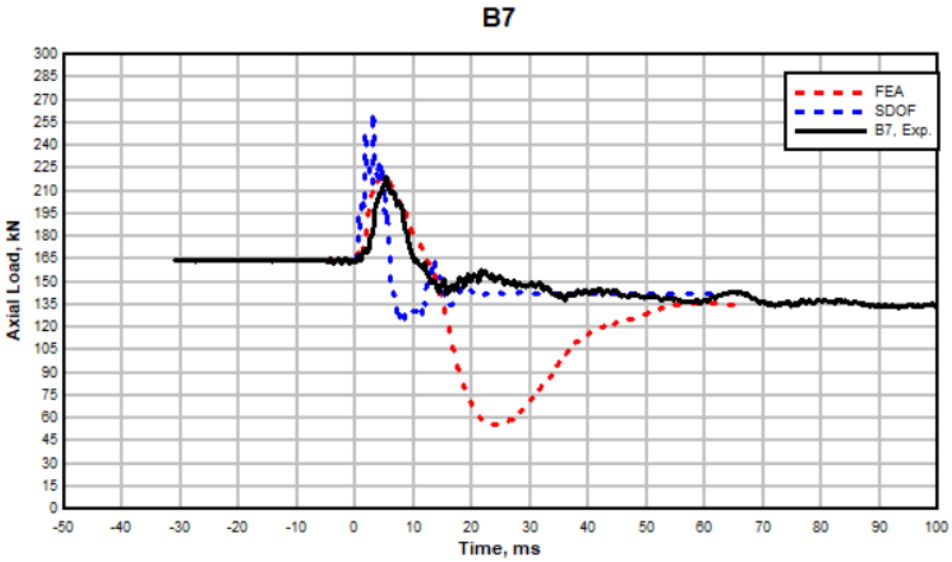

Figure 33: Comparison of the axial load from the test and analyses for B7 test.

8.2.4 Summary

To determine the performance of SDOF solution, the maximum deflections for the tests from [14-15] are compared. The comparison of the maximum displacement as a function of the charge size is shown in Fig.34 between the test and SDOF results for various axial loading condition. Both the simulation and the experiments show that the axial load will have significant effect on the deflection of the test object under the blast loading condition.

For Test Series 1 [14], the comparison is shown on the left hand side of Fig.34 for the test results as symbols and the analytical results as piecewise lines. For this test series, the SDOF solution seems to slightly overestimate the deflection for the test objects without the axial load. The SDOF deflection for the axially loaded tests shows to be smaller than those from the measurements.

Part of the reason for the underestimation of the bending deflection may be due to the difference in the applied axial loads. As mentioned previously, the axial load in the SDOF solution is based on the gravity of a mass on the top of the test object while the axial load is introduced on the test object with a hydraulic actuator. At the test condition, the axial force will be affected by the stiffness of the rig, the hydraulic oil, as well as the mass of the components. Compared to a mass with similar initial axial force, the test setup may have less inertia force against the axial movement, with resulting lower dynamic force and larger bending deflection. A test configuration with a mass on the top of the test object may be a better solution. Unfortunately due to the limitation of the test facility, the arrangement with a dead weight on top of the test object is not feasible.

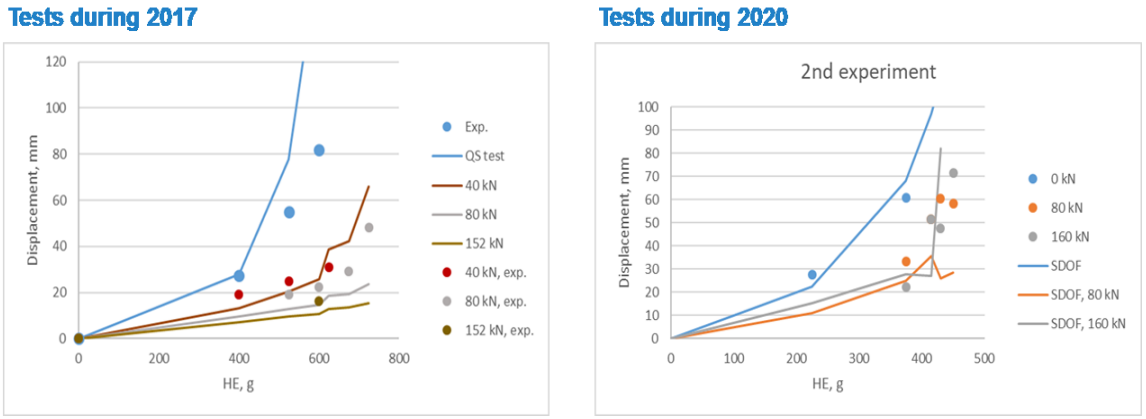

Figure 34: Comparison of the maximum deflection between the experiments (dot symbols) and the simulations (lines). The left hand side is for the tests from [14] and the right hand side is for the tests from [15].

For Test Series 2 [15], the blast load has a relatively higher peak pressure and lower impulse density (see the comparison in Fig.18). The comparison of the maximum bending deflection as a function of the charge size is shown on the right hand side of Fig.34, again with the test results as symbols and the analytical results as the piecewise lines.

For this test series, the peak pressure is generally higher than that for Test Series 1 as shown in the comparison in Fig.18 with the blue symbols. In this case for the test without the axial load, the SDOF solution results in a reasonable maximum deflection, compared to the experimental results, see Fig.34. The measured strength of the concrete is lower. The SDOF solution is shown as the curves in the right hand side of Fig.34. The result indicates shear failure for the charge size larger than 375g both at the initial axial load of 80 kN and 160 kNs.

According to eq.(75), the shear span reduces in a reverse proportion to the square root of the maximum pressure. Increase in pressure will shorten the shear span and increase the likelihood for shear failure. In addition, the shear span is also proportional to the square root of the sectional moment capability (eq.(75)). For the wall with the concrete of lower strength, the shear span will be further reduced. With these factors, the shear failure will likely occur for Test Series 2 when the axial load is applied, with the resulting lower sectional moment capability (see Fig.8 for the interaction diagram).

9 Conclusions

In this work, a solution for the response of the gravity loaded wall element subjected to a blast load is developed. The solution is based on the extension of the conventional single-degree-of-freedom (SDOF) method for the analyses of dynamic response of the structural components with significant dynamic axial load. With this solution, the gravity load is applied on the top of a wall with an equivalent mass. Under the dynamic event, the axial inertia effect of the mass is accounted for. Both the bending and shear failure behavior are included in the solution with the added effect due to the axial load. This solution is validated with some FEA simulations and experimental data to explore its potential for the general engineering evaluation of the dynamic response of a wall subjected to a blast load.

It is shown that, as a general fast-runing engineering solution, the solution is relatively robust and agrees reasonably well with the limited tests and FEA simulations.

10 References

[1] Hognestad, E. (1951). “A Study of Combined Bending and Axial Loads in Reinforced Concrete Members”, In Bulletin Series No. 399, University of Illinois Engineering Experimental Station.

[2] Haitham Al-Thairy, (2018). “Behaviour and Failure of Steel Columns Subjected to Blast Loads: Numerical Study and Analytical Approach” Advances in Materials Science and Engineering Volume, Article ID 1591384, 20 pages.

[3] Al-Thairy, H. and Wang,Y. C., (2011). “A numerical study of the behaviour and failure modes of axially compressed steel columns subjected to transverse impact,” International Journal of Impact Engineering, vol. 38, no. 8-9, pp. 732–744.

[4] Chen, F. L. and Yu, T. X., (2000). “Influence of axial pre-load on plastic failure of beams subjected to transverse dynamic load,” Key Engineering Materials, vol. 117–180, pp. 255–260.

[5] McConnell, J. R., Brown, H., ((2011)). “Evaluation of progressive collapse alternate load path analyses in designing for blast resistance of steel columns”, Engineering Structures v33 pp.2899–2909.

[6] Ronald L. Shope (2006), “Response of wide flange steel columns subjected to constant axial load and lateral blast load”. Civil Engineering Department, Blacksburg, Virginia.

[7] Shope, R. L., (2006). “Response of wide flange steel columns subjected to constant axial load and lateral blast load,” Ph.D. thesis, Faculty of the Virginia Polytechnic Institute and State University, Blacksburg, VA, USA.

[8] Abedini, M., Mutalib, Raman, A., S., Baharom, S., and Nouri, J., (2017), "Prediction of residual axial load carrying capacity of reinforced concrete (RC) columns subjected to extreme dynamic loads," Am J Eng Appl Sci, vol. 10, pp. 431-448.

[9] Astarlioglu, S., Krauthammer, T., Morency, D. and Tran, T.P., (2013), “Behavior of reinforced concrete columns under combined effects of axial and blast-induced transverse loads”, Engineering Structures, Vol. 55, pp. 26-34.

[10] Mohammad Esmaeilnia Omran and Somayeh Mollaei, (2017). “Investigation of Axial Strengthened Reinforced Concrete Columns under Lateral Blast Loading”, Shock and Vibration Volume 2017, Article ID 3252543, 18 pages.

[11] Paik J.K., Satish Kumar Y.V., Lee J.M. (2005), "Ultimate strength of cracked plate elements under axial compression or tension." Thin-Walled Struct 43.2 pp.237–272, https://doi.org/10.1016/j.tws.2004.07.010.

[12] Marcin P. BUDZIAK, Tomasz GARBOWSKI, (2014). “Failure Assessment of Steel-Concrete Composite Column Under Blast Loading”, ENGINEERING TRANSACTIONS Engng. Trans. V62, n1, 61–84.

[13] Crawford, J. E. Malvar, L. J. Morill, K. B., and Ferritto, J. M. (2001) “Composite retrofits to increase the blast resistance of reinforced concrete buildings.” Proc., 10th Int. Symp. On Interactin of the Effect of Munitions with Structures, Structural Engineer, San Diego, pp. 1-13.

[14] Berglund, R. and Hansson, H., (2017), “Experiments of axially loaded walls for urban damage assessment”, FOI-R--4394--SE, ISSN 1650-1942, FOI, Stockholm.

[15] Hansson, H. and Berglund, R., (2020), “Experimental investigation of axially loaded wall elements”, FOI-R--5108--SE, ISSN 1650-1942, FOI, Stockholm.

[16] fib “Model Code for Concrete Structures”, (2010), ISBN: 978-3-433-03061-5.

[17] Edin, K. and Forsen, R., (1991), ”Vapenverkan mot flervånings betongbyggnad II”, FOA Rapport C 20859-2.3 Dec.

[18] Wang, G. S., and Hansson, H., (2015), “Numerical Analyses of Fracture and Failure of Reinforced Concrete Components under Dynamic Loading Conditions”, FOI-R--4119--SE, FOI, Stockholm.

[19] Wang, G. S. (2016), “Numerical Modelling of P-I Response of Concrete Components Subjected to Air Blast Loading”, FOI-R- -4322- -SE, FOI, Stockholm, Nov.

[20] Wang, G. S. (2019), “Analyses and Simulations of Axially Loaded RC Walls Subjected to Airblast Load”, FOI-R- -4886- -SE, FOI, Stockholm, Dec.

[21] Newmark, N. M. (1950), “Methods of analysis for structures subjected to dynamic loading”, University of Illinois, Urbana, Illinois (Dec. 1950).

[22] Norris, C. H., Hansen, R. J. Holley, M. J., Biggs, J. M., Namyet, S., and Minami, J. V. (1959), “Structural design for dynamic loads”, McGraw-Hill Book Company, New York, New York.

[23] Biggs, J. M. (1964), “Introduction to structural dynamics”, McGraw-Hill Book Compancy, New York, New York.

[24] U. S. Army corps of engineers manual EM 1110-345-415 (1975),” Design of structures to resist the effects of atomic weapons”.

[25] Baker, W. E., Cox, P. A., Westine, P. S., Kulesz, J. J., and Strehlow, R. A. (1983), “Explosion hazards and evaluation”, Elsevier Scientific Publishing Company Inc. New York.

[26] Hughes, G. and Beeby, A. W. (1982). “Investigation of the effect of impact loading on concrete beams”, The Structural Engineer, vol.60B, No.3, 45-52.

[27] Magnusson, J., (2019), “Shear in concrete structural elements subjected to dynamic loads”, Doctoral thesis in civil and architectural engineering, KTH Royal Inst. of Tech. Stockholm.

[28] Kani, G. N. J. (1966), “Basic facts concerning shear failure”, J. ACI; 63, 675-692.

[29] Kani, G. N. J. (1967), “How safe are our large reinforced concrete beams”, J. ACI; 64 (3), 128-141.

[30] Timoshenko, S. (1928), “Vibration problems in engineering”, D. Van Nostrand Company, Inc., New York, New York.

[31] Galef, A. “Bending frequencies of compressed beams”, J Acoust. Soc. Am. 1968;44(2):643.

[32] Bokaian, A. (1988), “Natural frequencies of beams under compressive axial loads”, J. Sound Vib, 126(1):49-65.

[33] Whitney, C.S. (1937), “Design of Reinforced Concrete Members Under Flexure and Combined Flexure and Direct Compression”, ACI Journal, March-April; 33, 483-498.

[34] American Concrete Institute (2011). “Building Code Requirements for Structural Concrete”, (ACI 318-11).

[35] Applied Techology Council and Building Seismic Safety Council, (1997).

[36] W. Griffel, “Handbook for formulas for stress and strain”, Frederick Ungar Publishing Co., New York, 1966.

FOI, Swedish Defence Research Agency, is a mainly assignment-funded agency under the Ministry of Defence. The core activities are research, method and technology development, as well as studies conducted in the interests of Swedish defence and the safety and security of society. The organisation employs approximately 1000 personnel of whom about 800 are scientists. This makes FOI Sweden's largest research institute. FOI gives its customers access to leading-edge expertise in a large number of fields such as security policy studies, defence and security related analyses, the assessment of various types of threat, systems for control and management of crises, protection against and management of hazardous substances, IT security and the potential offered by new sensors.

FOI
Defence Research Agency
SE-164 90 Stockholm

Phone: +46 8 555 030 00
Fax: +46 8 555 031 00

www.foi.se